Exploring Charge Transport in High-Temperature Polymorphism of ITIC Derivatives in Simple Processed Unipolar Bottom Contact Organic Field-Effect Transistor

Yatzil Alejandra Avalos Quiroz, Tomoyuki Koganezawa, Pavlo Perkhun, Elena Barulina, Carmen Ruiz Herrero, Jörg Ackermann, Noriyuki Yoshimoto, Christine Videlot-Ackermann

Exploring charge transport in high temperature polymorphism of ITIC derivatives in simple processed unipolar bottom contact organic field-effect transistor

Yatzil Alejandra Avalos Quiroz, Tomoyuki Koganezawa, Pavlo Perkhun, Elena Barulina, Carmen M. Ruiz, Jörg Ackermann, Noriyuki Yoshimoto, Christine Videlot-Ackermann**

Y. A. Avalos Quiroz, Dr. P. Perkhun, Dr. E. Barulina, Dr. J. Ackermann, Dr. C. Videlot-Ackermann
Aix Marseille Univ., UMR CNRS 7325, CINaM, 13288 Marseille, France.
E-mail: videlot@cinam.univ-mrs.fr

Dr. T. Koganezawa
Industrial Application Division, Japan Synchrotron Radiation Research Institute (JASRI), Sayo, Hyogo 679-5198, Japan.

Dr C. M. Ruiz
Aix Marseille Univ.,Univ. de Toulon, UMR CNRS 7334, IM2NP, Marseille, France

Prof. N. Yoshimoto
Department of Physical Science and Materials Engineering, Iwate University, Ueda Morioka 020 8551, Japan.
E-mail: yoshimoto@iwate-u.ac.jp

Keywords: Non-fullerene acceptors, thin film transistors, dielectric passivation, thermal stability, polymorphism, electron mobility, J-aggregate.

Abstract

Power conversion efficiency of organic solar cells increases continuously due the emergence of novel non-fullerene acceptors (NFAs). As solar cell efficiency is governed by photogeneration followed by charge carrier transport towards the electrode, understanding of univocal electron transport properties of NFAs is of great importance. Acceptors from the indacenodithienothiophene (IDTT)-based family such as ITIC, ITIC-Th and ITIC-4F have been intensively studied in solar cells. Importantly ITIC and ITIC-4F based films evolve with increasing annealing temperature from 100°C up to 250°C into several polymorphs that may impact the electronic transport strongly. Here we study for the first time the effects of temperature depending polymorphism on the charge transport properties of ITIC, ITIC-Th and ITIC-4F. We first develop an unipolar, high performance and high temperature stable thin film transistor structure using divinyltetramethyldisiloxane-bis(benzocyclobutene) BCB as dielectric passivation material to explore the intrinsic charge transport up to 240°C. We show that electron mobility in the three ITIC-based films is strongly influenced by the molecule specific polymorphism at optimal temperatures. This leads to a strong increase in electron mobility compared to the as-cast films, which is correlated to changes in molecule aggregation, domain crystallinity and orientation as well as intermolecular electronic coupling.

1. Introduction

The emergence of novel non-fullerene acceptors (NFAs) has resulted in a significant increase in the power conversion efficiency (PCE) of organic solar cells in recent years beyond 17% for single-junction devices.[1] Compared to fullerene-based acceptors, NFAs have advantages in meeting essential requirements for high PCEs such as a reduced energy loss for a high open-circuit voltage (V_{OC}) and an extended absorption range for a high short-circuit current density (J_{SC}).[2] Fused-ring electron acceptors (FREAs) composed of an electron donating central

aromatic fused ring and terminal electron withdrawing units leading to so-called acceptor–donor–acceptor (A–D–A) molecules are today the most common and efficient NFAs.[3] FREAs based on indacenodithienothiophene (IDTT) core such as 3,9-bis(2-methylene-(3-(1,1-dicyanomethylene)-indanone))-5,5,11,11-tetrakis(4-hexylphenyl)-dithieno[2,3-d:2',3'-d']-s-indaceno[1,2-b:5,6-b']dithiophene (ITIC) (**Figure 1a**) reported first by Zhan *et al.*[4] have attracted considerable attention as organic semiconductors (OSCs) to achieve impressive PCEs of 9-13%,[5] and are today one of the most studied NFAs. They can easily be chemically modified, including halogenation and side chain engineering as 3,9-bis(2-methylene-(3-(1,1-dicyanomethylene)-indanone))-5,5,11,11-tetrakis(5-hexylthienyl)-dithieno[2,3-d:2',3'-d']-s-indaceno[1,2-b:5,6-b']dithiophene (ITIC-Th) and 3,9-bis(2-methylene-((3-(1,1-dicyanomethylene)-6,7-difluoro)-indanone))-5,5,11,11-tetrakis(4-hexylphenyl)-dithieno[2,3-d:2',3'-d']-s-indaceno[1,2-b:5,6-b']dithiophene (ITIC-4F) (Figure 1a), to change their electronic properties, optical band gap, crystallinity and solubility.[6] The concomitant effect of a planar backbone and large conjugated structure allows FREAs to form an ordered π-π intermolecular stacking in thin films and, unlike ball fullerenes, greatly affects their charge transport capability.[7] Depending on the growth conditions of ITIC single crystals, two distinct packing motifs have been identified: a face-to-face and an edge-to-face.[7b,7c,8] Thus ITIC crystal is characteristic of one-dimensional stacking, while ITIC films show three-dimensional molecular packing through local π-π stacking interaction between the terminal acceptor end-groups. Importantly due to their specific A–D–A structure, theses FREAs can form a large pallet of molecule stacking in layers. Recently, it was found that ITIC and ITIC-4F based films structurally evolve with increasing annealing temperature from 100°C up to 250°C into several polymorphs.[9] Different polymorphs, even with the slightest changes in their molecular packing may impact the electronic properties by orders of magnitude. However, the effects of these temperatures-induced changes in polymorphism on the charge transport properties of NFAs have not yet been investigated in depth. Since some of the observed high-temperature

polymorphisms require a temperature above 200°C, it is important to use a robust and thermal annealing resistant set-up dedicated to the measurement of charge transport. Organic thin-film transistors (OTFTs), are commonly employed to determine the charge transport properties of component thin films.[10] Majority of OTFTs are built as the bottom gate structure based on silicon dioxide (SiO_2) grown on n-doped silicon wafers because of an ease in deposition of active material on the insulator. There are two different OTFT designs using a bottom gate, the bottom gate top contact (BGTC) structure and the bottom gate bottom contact (BGBC). Usually the BGTC outperformed the BGBC structure due to a lower injection contact resistance and a higher current density.[11] However, the BGBC structure is, in terms of simplicity of use in a laboratory and material screening, more suitable, as there is no need for thermal evaporation of the top contacts on the transport material. In both structures, the surface of the dielectric layer plays an important role in governing the charge transport process in OTFTs.[12] Especially for acceptor materials such as ITIC series, various treatments as octyltrichlorosilane (OTS), poly(2,3,4,5,6-pentafluorostyrene (PPFS) or divinyltetramethyldisiloxane-bis(benzocyclobutene) (BCB) have been used to modify the SiO_2 gate dielectric surface.[13] OTS-modified BGBC OTFTs demonstrate an ambipolar transport, *i.e* the appearance of both n- and p-channels.[13a] To our knowledge, no unipolar BGBC structure has been reported so far. Unipolar transport has been only measured in the case of BCB or PPFS in BGTC structure with selected low W_f metals as aluminum or calcium vacuum deposited as top electrodes.[13b,13c] Interestingly, BCB is an amorphous insulating polymer (resistivity, $\rho = 10^{19}$ Ω/cm), nonpolar (dielectric constant, $\varepsilon_r < 3.5$), hydrophobic, employed in interface engineering and suitable for electron-transporting with various device configurations.[14] Most importantly, BCB has a glass transition $T_g > 300$°C and a decomposition temperature up to 350°C which makes it particularly adapted for measurements on charge transport in thin films annealed at high temperature.

In the present study, we present an unipolar, high performance and high temperature stable BGBC OTFT structure allowing exploring the intrinsic charge transport of ITIC and its

derivatives, ITIC-Th and ITIC-4F, using post-annealing temperature up to 240°C. The advanced electronic resin BCB deposited as a thin layer on silicon oxide substrate is demonstrated to be a superior dielectric treatment compared to silanization process based on OTS and hexamethyldisilazane (HMDS) (see chemical structures in **Figure S1**). Combined with Au electrodes modified by grafting of 4-(dimethylamino) benzenethiol (DABT), BCB is integrated here as capping and passivating layer to generate BGBC OTFTs that not only show high quality unipolar electron transport and high $I_{on/off}$ ratio, but also a higher temperature stability in combination with high mobility values. This allows us to explore the high temperature polymorphs of ITIC series. The thermal induced changes in electron mobilities are correlated to the accompanying modification in thin film absorption, morphology and microstructure of ITIC derivatives. Contact angle measurements and atomic force microscopy (AFM) were used to study the surface treatment, while OTFT measurements were correlated with absorption spectroscopy, AFM and grazing incident wide angle X-ray scattering (GIWAXS) to draw clear structure-property relationships. We demonstrate first the unique unipolar performance of BCB processable BGBC OTFTs up to temperatures of 240°C. Then by applying this advanced device structure to FREAs layers, we study the evolution of intrinsic electron mobility of the three OSCs as a function of the post-annealing temperature. Our results reveal that charge transport in thin films is strongly influenced by the annealing temperature that induces molecule specific polymorphism. Indeed, optimal annealing temperatures are found specifically for each ITICs leading to a general variation in electron mobility of more than one order of magnitude. We then correlate electron mobility to molecule aggregation, domain crystallinity and orientation demonstrating that the intrinsic transport in the three FREAs depends mainly on degree of molecule ordering and J-aggregates together with intermolecular electronic coupling and is less affected by the molecular planes orientation such face-on or edge-on orientation inside the channel. Compared to alkyl chains substitution used

in ITIC-Th fluorination in ITIC-4F leads to the highest electron mobility of 3.7×10^{-2} $cm^2/V.s$ at 200°C due to a highly ordered J-aggregate with enhanced intermolecular interaction.

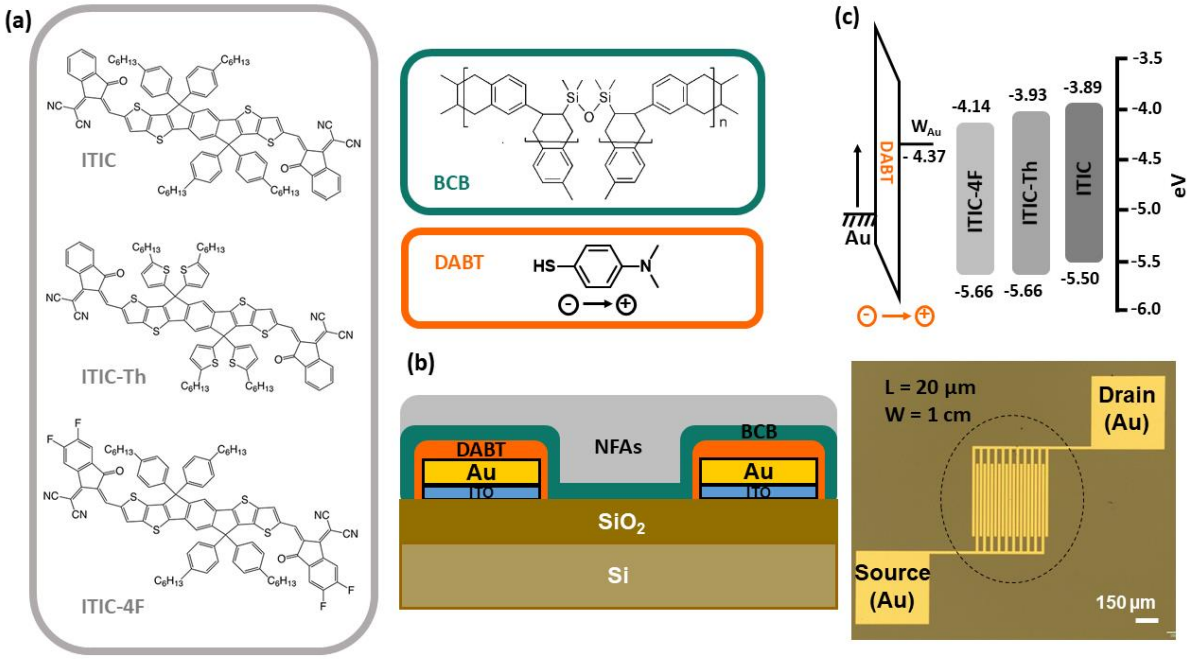

Figure 1. Chemical structure of NFAs (ITIC, ITIC-Th and ITIC-4F) as small organic semiconducting materials, BCB as a modifying agent for dielectric surfaces, and DABT as a modifying agent for gold electrodes (a). Schematic cross-section of the operating n-type OTFT in bottom gate bottom contact (BGBC) structure together with a top view of interdigitated source and drain electrodes, channel width (W) of 1 cm and channel length (L) of 20 µm (b). Schematic of energy levels for modified Au and NFAs (c).

2. Results and discussion

2.1 Development of an unipolar high temperature stable BGBC OTFT structure

The chemical structures and energy levels of the three FREAs (ITIC, ITIC-Th and ITIC-4F) investigated in this work are shown in **Figure 1**. All FREAs has a common IDTT electron donating central aromatic fused ring and two terminal electron withdrawing units based on the 1,1-dicyano-methylene-3-indanone (IC) to form an A–D–A arrangement. The main difference is either in the nature of the side chain, where the phenylhexyl side chains in ITIC are replaced by thienylhexyl chains in ITIC-Th or in the end-group fluorination in ITIC-4F. The highest

occupied molecular orbital (HOMO) and the lowest unoccupied molecular orbital (LUMO) levels of ITIC are −5.50/−3.89 eV.[5] Its fluorinated counterpart ITIC-4F shows lowered HOMO/LUMO levels, being −5.66/−4.14 eV due to the strong electron-withdrawing ability of F atoms, which enhances the push−pull effect between the core unit and the terminal groups.[5] Fluorination therefore reduces the LUMO level and electronic band gap of NFAs.[15] Compared to ITIC, ITIC-Th shows lower energy levels (HOMO/LUMO: −5.66/−3.93 eV) due to the σ-inductive effect of thienyl side-chains, with an intermediate LUMO level among the three compounds.[16] With a W_f of -4.83 eV, bare Au source (S) and drain (D) electrodes are unsuitable for efficient electron injection into the LUMO levels of ITIC series. Grafting of a thiol derivative, as DABT, onto the gold surfaces in the bottom contact structures has been found to decrease W_f to -4.37 eV for modified-electrodes.[17] DABT was shown to be the most promising thiol derivative to improve the performances and the electrical stability of both p- and n-channel OTFTs.[18] By choosing DABT as Au surface passivation agent, an induced proper alignment of the source-drain electrode W_f with the LUMO level of the ITICs promotes thus efficient electron injection/collection at the modified Au electrodes.

Concerning the passivation of SiO_2 dielectric layers, we applied HMDS, OTS or BCB (see chemical structures on **Figure S1**). HMDS and OTS are deposited using standard procedure of dip-coating, while a thin BCB layer is processed by spin-coating on top of the DABT-treated Au-electrodes.The BCB thin film is then cross-linked at 250°C on a hot plate for 1 h leading to a 3.5 nm thick passivating layer with a total capacitance per unit area of BCB-modified SiO_2 substrates of 18.8×10^{-9} $F.cm^{-2}$. HMDS and OTS-modified SiO_2 substrates show the same capacity with a value of 14.5×10^{-9} $F.cm^{-2}$ and close to that of pristine SiO_2 (14×10^{-9} $F.cm^{-2}$). Contact angle measurements reveal that BCB leads to passivated SiO_2 surfaces with a contact angle (WCA) of 90° compared to 52° for pristine SiO_2 dielectric that is clearly lower compared to HMDS and OTS-modified SiO_2 substrates with higher WCAs between 93°-96° (**Figure S1**).

We then compare the electrical responses of as-cast ITIC in BGBC OTFTs using the three different SiO_2 passivations under stringently identical processing conditions for ITIC films. Regarding first the impact of the DABT treatment only, we note that pristine SiO_2-based OTFT devices deliver an ambipolar transport with a dominant hole-transport under negative bias, while the DABT treatment generates an unipolar electron transport with a well-defined injection under positive bias (**Figure S2**). With a work function of DABT-modified electrodes close to LUMO levels of ITICs, an efficient electron injection occurred in BGBC OTFT devices. Applying then the additional dielectric treatment (**Figure S3** and **S4**), only the BCB-treated transistors show a perfectly unipolar electron transport (accumulation in positive bias and depletion in negative bias). Although the injection is slightly disturbed by the presence of the BCB coating the electrodes as it can be seen from the slower current rising at low voltages, OTFTs deliver a high drain current in the saturation regime with a well-defined accumulation. Comparing the extracted electron mobility in the saturation regime for as-cast films show that the highest mobility of 3.1×10^{-3} $cm^2/V.s$ is obtained for BCB-modified OTFTs compared to HMDS and OTS passivation with lower mobility values of $1.4\text{-}1.5\times10^{-3}$ $cm^2/V.s$ (**Figure 2** and **Table S1**). With only DABT-modified electrodes, the mobility is even an order of magnitude lower with 1.3×10^{-4} $cm^2/V.s$. Together with the unique unipolar transport, this makes BCB-modified OTFTs clearly advantageous compared to the two common silanization techniques.

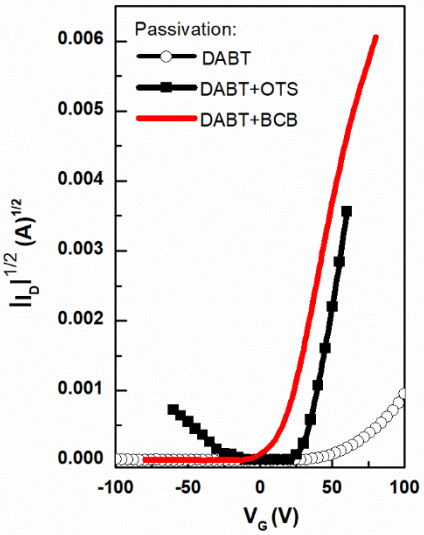

Figure 2. Transfer characteristics of as-cast ITIC films in BGBC OTFTs versus different passivations. (DABT: with only DABT-treated gold electrodes, DABT+OTS: DABT-treated gold electrodes and OTS-modified SiO_2, DABT+BCB: DABT-treated gold electrodes and BCB-modified SiO_2).

As we aim to study charge transport properties of ITIC series at high temperatures up to 240°C, we also studied the thermal stability of the BGBC OTFT structures versus SiO_2 passivation. While HMDS and OTS surface treatments can be considered as stable under thermal stress up to 200-250°C,[19] the weak point of the salinized BGBC structures is the DABT monolayer that starts to desorb easily under thermal annealing.[17] To investigate the thermal stability of BGBC structure, we compared ITIC-based devices with as-cast and thermally annealed layers at 240°C. DABT-treated OTFTs using OTS or HMDS still demonstrate an ambipolar transport but with the addition of a non-ideal saturation as shown in **Figure S5**. While a slight increase in electron mobility of 2.4-4.9×10^{-3} cm^2/V is measured (**Table S1**), a sharp increase in V_t and a loss of saturation behavior at $V_D > V_G$ are observed highlighting a clear degradation of the transistor response under thermal annealing. These changes can be attributed directly to thermal instability of DABT monolayer formed on Au surface as shown on **Figure S6** when only DABT was used to treat the electrodes. DABT is therefore identified as a limiting factor for the process

design of organic electronic devices in which substrate heating is required.[17] In the case of BCB as surface passivation of SiO_2, the BCB layer is deposited on top of the DABT monolayer bearing gold contacts as shown in **Figure 1**. It is important to mention that the processing of the BCB as SiO_2 passivation layer requires a 250°C annealing step over 1 h exposing thus the DABT monolayer to high temperature over the same time period already prior to the deposition of the active layer. **Figure S7** shows the output and transfer characteristics of ITIC-based OTFTs in BGBC post-annealed at 240°C with BCB-modified SiO_2 and DABT-treated gold electrodes. Thermal annealing OTFTs reveals not only a well-defined saturated regime but also a clearly improved unipolar transport regime demonstrating that BCB stabilizes the DABT layer. More importantly, the high temperature annealed devices show identical clear characteristics with, additionally, enhanced current densities corresponding to an increase in electron mobility by a factor of 4 to reach 1.3×10^{-2} cm^2/V (**Table S1**). Such a strong enhancement of mobility was not observed for the BGBC OTFTs treated with OTS or HMDS. This may be related to the fact that BCB layers are not only extremely flat with a surface roughness of 0.4 nm (**Figure S8**) but also the WCA value of BCB is very close to that of the FREAs such as ITIC-4F of 89° compared to OTS or HMDS surface with values clearly higher around 93°-96° suggesting a beneficial effect of similar surface energies and thus enhanced molecular ordering under thermal annealing in the case of BCB passivation.[6c]

2.2 Temperature depending charge transport of FREAs using BCB passivated BGBC OTFTs

After successful demonstration of the high performance and temperature stability of the new BCB-passivated BGBC OTFT test structure, we explore here in detail the intrinsic charge transport properties of the ITIC series in as-cast and thermally annealed films between 100°C

and 240°C by extracting mobility (μ), threshold voltage (V_T), on/off current ratio (I_{on}/I_{off}) in the saturation regime of the transfer characteristics as shown in **Table 1**.

For as-cast thin films, ITIC-Th based OTFTs delivered the highest electron mobility with a value of 5.5×10^{-3} $cm^2/V.s$, a threshold voltage of 17.6 V and a I_{on}/I_{off} of 0.2×10^6, while ITIC-4F shows the lowest mobility of 1.2×10^{-3} $cm^2/V.s$ and ITIC an intermediate value of 3.1×10^{-3} $cm^2/V.s$. A general increase in electron mobility from ITIC to ITIC-Th by changing from phenylhexyl side chains to thienylhexyl chains has been previously assigned to enhanced intermolecular interactions on inclusion of the sulfur containing thiophene unit in the side chain.[20] However the mobility values for as-cast films may be limited not only by the molecular structure, but also by morphological parameters such as crystal ordering that is discussed later. It is interesting to highlight that the extracted mobility values of $3\text{-}5.5\times10^{-3}$ $cm^2/V.s$ (or $\mu_{eff} = 1.1\times10^{-3}$ $cm^2/V.s$ as calculated later) for ITIC and ITIC-Th, respectively, are even higher than those obtained on PPFS fluorinated polymer dielectrics in BGTC structure demonstrating the superior performance of the developed here BCB-passivated BGBC OTFT structure.[13b] The electron mobility values in thin film obtained in the present study are very close to those obtained by atomistic molecular dynamics simulations on ITIC thin film (4.6×10^{-3} $cm^2/V.s$) where a three dimensional molecular packing is formed through local intermolecular π−π stacking between the terminal acceptor units.[8] To study the electron transport in the FREA films in the high temperature regime, the complete BGBC OTFTs included as-cast FREA layers were annealed from 100°C to 240°C during 10 minutes. **Figure 3** shows the resulting evolution of the extracted electron mobility μ as function of the applied annealing temperature where several key results can be drawn. First, the charge transport for the three FREAs changes strongly with increasing temperature, but the highest mobility is achieved for molecule-specific temperatures, which do not necessarily correspond to the highest temperature of 240°C. Indeed, the electron mobility of ITIC reaches a maximum at 240°C, while those of ITIC-Th and ITIC-4F show a maximum at 150°C and 200°C, respectively, before decreasing both for higher

temperatures. We also see that there are weak fluctuations in electron mobility when annealing below the optimal temperature. Indeed the electron mobility in ITIC and ITIC-Th films decreases at 180°C as already observed for ITIC by Kippelen *et al*.[13c] Furthermore although ITIC-4F shows the lower mobility in as-cast films, thermal annealing at 200°C leads to the highest mobility value with 3.7×10^{-2} $cm^2/V.s$ (**Figure 4**). Importantly this corresponds to an increased electron mobility by approximately a factor of 30 indicating that post-annealing strongly enhances the charge transport in these layers towards the highest electron mobility for such FREAs.

As mentioned above, the injection is slightly disturbed by the presence of the BCB coating the electrodes implying non-ideal transfer characteristics at low gate voltage due to a substantial threshold. To ensure the reliability of mobility extraction, the effective carrier mobilities (μ_{eff}) have been estimated by using the measurement reliability factor r for the three FREAs with $\mu_{eff} = \mu \times r$ where μ is the extracted mobility.[21] **Figure S9** shows detailed transfer curves of pristine and post-annealed ITIC-4F in BGBC OTFTs with BCB-modified SiO_2 and DABT-treated gold electrodes with r factors in the saturation regime calculated to 57% and 43%, respectively. **Figure S10** compares the effective carrier mobility μ_{eff} to the extracted mobility μ for the different post-annealing temperatures of thin films with measurement reliability factors, r, of 33-43% for ITIC, 35-50% for ITIC-Th and 43-61 % for ITIC-4F. After applying the r factor, post-annealed ITIC-4F based OTFTs still deliver the highest mobility with values superior to 1×10^{-2} $cm^2/V.s$. While the effective mobility values are slightly lower than extracted one, the overall temperature evolution is conserved proving that the charge transport in these films strongly depends on the temperature-induced morphology. Therefore, we focus in the next part on detailed analyses of the impact of the thermal annealing on the molecule ordering in thin films.

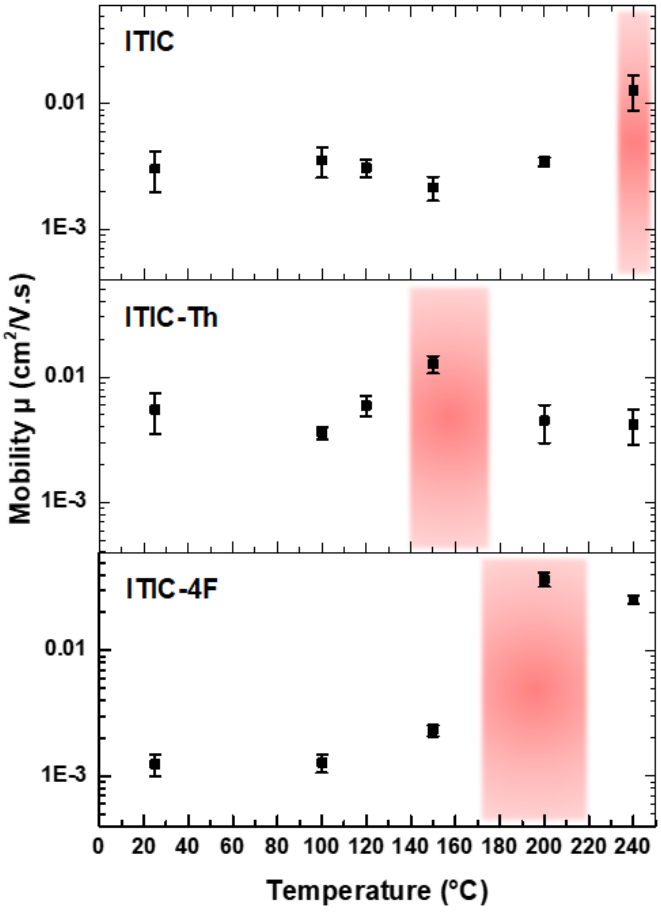

Figure 3. Extracted mobility values μ of ITIC, ITIC-Th and ITIC-4F for different post-annealing temperatures of the thin films. The colored area corresponds to the more ordered crystallinity feature according to the applied annealing temperatures range.

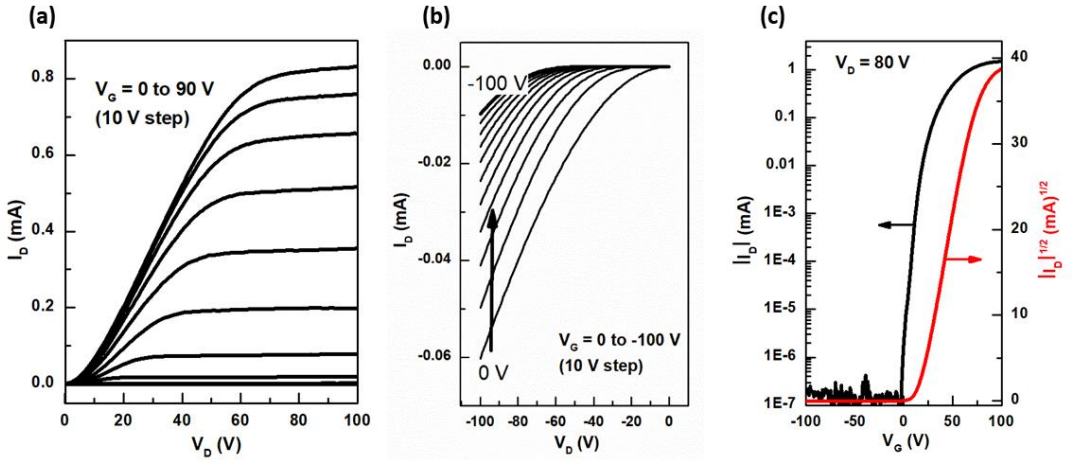

Figure 4: Output (a,b) and transfer (c) characteristics of ITIC-4F films post-annealed at 200°C in BGBC OTFTs with DABT-treated gold electrodes and BCB-modified SiO_2 dielectric.

Table 1. Electron transport parameters of ITIC, ITIC-Th and ITIC-4F evaluated in BGBC OTFTs based on DABT-treated gold electrodes and BCB-modified SiO_2 dielectric.

Active materials	*Temp (°C)*	*μ (cm^2/V.s)*	*V_T (V)*	*I_{on}/I_{off}*
ITIC	as-cast	$3.1 \pm 1.1\times10^{-3}$	16.6 ± 5.4	0.5×10^6
	100	$3.6 \pm 0.9\times10^{-3}$	14.2 ± 1.8	0.3×10^6
	120	$3.1 \pm 0.5\times10^{-3}$	15.8 ± 2.2	0.4×10^6
	150	$2.2 \pm 0.4\times10^{-3}$	23.6 ± 3.1	0.4×10^6
	200	$3.4 \pm 0.3\times10^{-3}$	20.5 ± 0.4	1.1×10^6
	240	$1.3 \pm 0.4\times10^{-2}$	15 ± 7.7	0.7×10^6
ITIC-Th	as-cast	$5.5 \pm 2\times10^{-3}$	17.6 ± 7.7	0.2×10^6
	100	$3.6 \pm 0.4\times10^{-3}$	13.8 ± 5.2	0.4×10^6
	120	$5.9 \pm 1\times10^{-3}$	22.4 ± 5.1	0.4×10^6
	150	$1.3 \pm 2\times10^{-2}$	15.2 ± 4.9	1.5×10^6
	200	$4.5 \pm 1.5\times10^{-3}$	17.8 ± 4.5	0.7×10^6
	240	$4.2 \pm 1.3\times10^{-3}$	21.7 ± 3.7	0.7×10^6
ITIC-4F	as-cast	$1.2 \pm 0.2\times10^{-3}$	9.5 ± 3.7	0.05×10^6
	100	$1.3 \pm 0.2\times10^{-3}$	11.8 ± 1.7	0.2×10^6
	150	$2.3 \pm 0.2\times10^{-3}$	11.4 ± 2.7	0.1×10^6
	200	$3.7 \pm 0.4\times10^{-2}$	13.1 ± 2.7	4.3×10^6
	240	$2.5 \pm 0.2\times10^{-2}$	9.6 ± 1.9	9.3×10^6

2.3 Correlation of thermal annealing and molecular ordering in FREA films

To correlate the electron mobility variation, especially at high annealing temperature range, with structural changes in the molecular ordering inside the layers, we combined a set of advanced techniques including AFM, temperature depending absorption spectra and GIWAXS to gain deeper structure-property relationships. The surface topography of ITIC, ITIC-Th and ITIC-4F thin films deposited on BCB-modified SiO_2 substrates was first characterized by AFM. **Figure 5** and **S11** compares the AFM images of the FREA layers annealed at 100°C corresponding to the low mobility range with those of layers annealed at the temperature leading to the highest charge transport, i.e. 240°C for ITIC, 150°C for ITIC-Th and 200°C for ITIC-4F,

respectively. The resulting surface morphology depends on both molecular structure and applied thermal temperature. Importantly due to their high decomposition temperatures (300°C) and a melting (endothermic) transition observed for ITIC-4F at 251°C, we can consider that the studied films are not degraded at high annealing temperatures up to 240°C and only change due to reorganisation of the molecules inside the films.[8b,22] At 100°C, AFM images of ITIC and ITIC-Th thin films show a rather amorphous surface with small grain structures of 40-100 nm size, while ITIC-4F layers are composed of much smaller domains (10-20 nm). This points towards a poorer ordering of ITIC-4F films compared to ITIC and ITIC-Th that goes in line with the observed lower electron mobility. Increasing annealing temperature leads to clear changes in the layer morphology. ITIC molecules form layers composed of large and densely packed grains showing some fibrillary structure at 240°C on a larger scale (**Figure S11**). In contrast, ITIC-Th and ITIC-4F films show enlarge but still small grains at 150°C and 200°C, respectively. In the case of ITIC-4F, a polycrystalline film composed of 20 nm diameter sized grains is clearly observed.

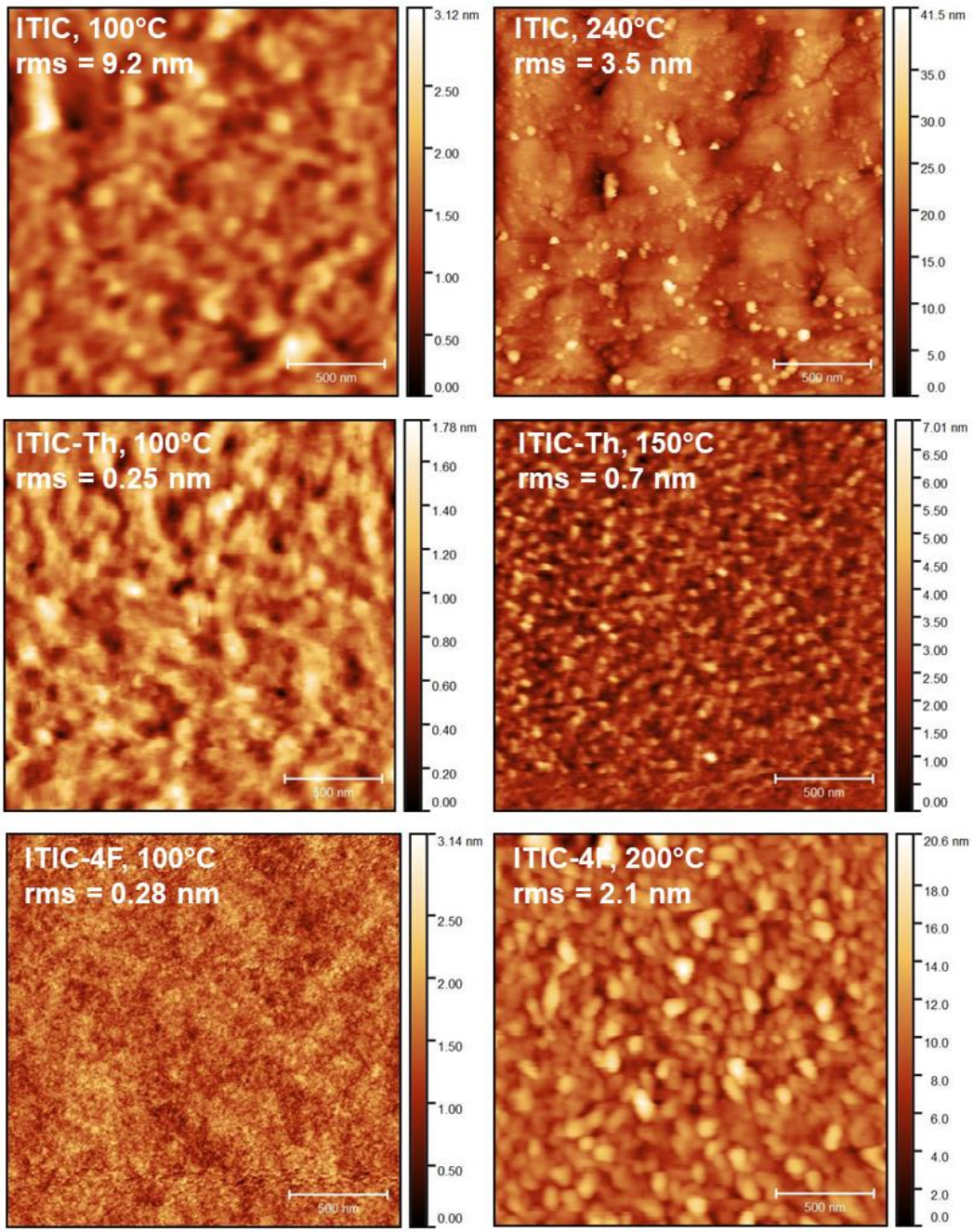

Figure 5. AFM topography images of ITIC, ITIC-Th and ITIC-4F n-type semiconductor molecules deposited on BCB-modified SiO_2 surfaces. (Scale 500 nm)

We then apply temperature-dependent absorption measurements to study temperature depending ordering of the molecules in thin films.[9] Corresponding UV-Vis spectra are shown in **Figure 6** with ITIC-4F as example, while **Figure S12** shows spectra of ITIC and ITIC-Th films, respectively. For the three FREAs, UV-Vis spectra of as-cast films exhibit two

transitions: a stronger one ($A_{0\text{-}0}$) at high wavelengths and a less intense ($A_{0\text{-}1}$) at shorter wavelengths.[9] In the case of ITIC-4F, the fluorination generates a stronger electron push-pull effect inducing a slightly red-shift of the absorption spectra with a $A_{0\text{-}0}$ peak at 724 nm compared to $A_{0\text{-}0}$ peak at 704-706 nm for ITIC and ITIC-Th. As recently reported for ITIC and ITIC-4F films, studying changes in the absorption spectra, i.e. $A_{0\text{-}0}$ peak position and full-width-half-maximum (FWHM) value together with the ratio of $A_{0\text{-}0}$ peak/$A_{0\text{-}1}$ peak (see **Figure 6b**) as a function of post-annealing temperature, allow to get insight in temperature depending polymorphs, molecule aggregation and crystallinity.[9] Here, we observe a continuous redshift of the $A_{0\text{-}0}$ peak for the three FREAs, however only for ITIC-4F there is an abrupt and pronounced shift position starting at 200°C suggesting a predominance J-type dimers in this case.[23] The evolution of the peak ratio $A_{0\text{-}0}/A_{0\text{-}1}$ is different for each material. In the case of ITIC, $A_{0\text{-}0}/A_{0\text{-}1}$ of as-cast films shows first an increase when annealing at 100°C followed by a decrease at 150°C. Further increase in temperature to 200°C again increases the peak ratio $A_{0\text{-}0}/A_{0\text{-}1}$ up to 240°C. As proposed by L. Ciammaruchi *et al.* ITIC seems to undergo different phase transition polymorph with a competition of J and H-aggregates.[9] In the case of ITIC-Th, we see an opposite trends, annealing at 100°C leads to a decrease of the $A_{0\text{-}0}/A_{0\text{-}1}$ ratio compared to as-cast films followed by a continuous increase up to 200°C followed by a decrease at 240°C. ITIC-4F films show first an unchanged ratio up to 150°C, while there is a sharp increase in the peak ratio $A_{0\text{-}0}/A_{0\text{-}1}$ at 200°C followed by the highest ratio amongst the three FREAs at 240°C pointing towards a high degree of J-like aggregates in ITIC-4F films.[23]

If we now compare the temperature-dependent evolution of the two parameters, $A_{0–0}/A_{0–1}$ ratio and FMHW of peak $A_{0\text{-}0}$, with the electron mobility measured inside the films, we see that they are relatively similar. This suggests that there is a strong correlation between J-aggregation and intermolecular coupling between the acceptor end-groups and high mobility regime. The FWHM value gives information about the ordering inside the films as a function of annealing temperature. As show in **Figure 6b** for as-cast films, ITIC-4F has the highest values

corresponding to the lower degree of crystal order, followed by ITIC, while ITIC-Th shows the smallest values and thus highest order (**Figure S12**). Annealing up to 200°C leads to a clear decrease in FHWM for the three FREAs indicating a strongly enhanced degree of ordering in the films. Importantly in the case of ITIC and ITIC-Th, FWHM values strongly increase again for 240°C pointing towards a loss of crystallinity. Latter may explain the loss in electron mobility for ITIC-Th in the high temperature regime. Based on a previous reported study, the highest mobility values for ITIC and ITIC-4F obtained here are situated into the temperature range where the crystallinity features show the most ordered phase with strong of J-like character (colored areas on **Figure 3**).[9] By analogy, a colored area was also added for ITIC-Th in the region associated with the highest mobility values. ITIC-4F shows highest interchain coupling, largest population of J-aggregates and ordered crystalline structure as shown before.[9] Together with the induced planarization of the oligomer backbone by the fluorination inducing a stronger π–π interaction between ITIC-4F this may be reason for higher mobility for ITIC-4F based OTFTs after a post-thermal treatment.[24]

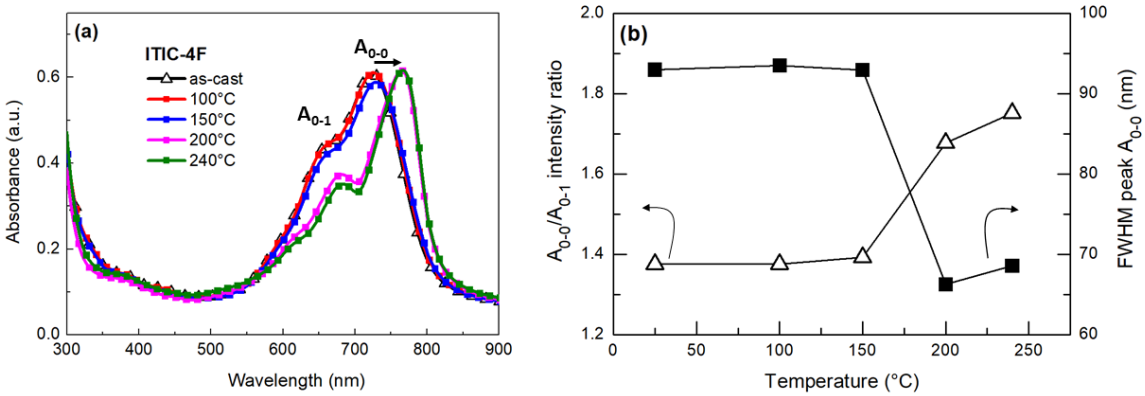

Figure 6. Absorption spectra (a) and A_{0-0}/A_{0-1} intensity ratio together with FMHW of A_{0-0} peak (b) for ITIC-4F thin films as function of the annealing temperature

In the next part, 2D-GIXD measurements are employed to study the molecular packing and crystallinity of the ITIC series based thin films more in details (**Figure 7** and **Figure 8**). We compare 2D diffraction patterns (q_{xy}, q_z) and the corresponding in-plane (IP) and out-of-plane (OOP) intensity profiles of 100°C annealed layers, which corresponds to the low mobility regime for the three FREAs, with the layers annealed at the temperature leading to the highest mobility (*i.e.* 240°C for ITIC, 150°C for ITIC-Th and 200°C for ITIC-4F). From **Figure 7** and **Figure 8** we see that in all cases thermal annealing enhances strongly the crystallinity of the films expressed by much brighter and sharper scattering peaks. At 100°C, ITIC molecules demonstrate a poor ordering degree with a predominant face-on molecular planes orientation highlighted by a broad π–π stacking peak (010) at q_z = 16.3 nm^{-1} in OOP profile with a stacking distance of 0.38 nm ($d = 2\pi/q$). The peak located at q_{xy} = 4.2 nm^{-1} (d = 1.5 nm) in the IP intensity profile is indexed (100) for the lamellar stacking in the IP direction. The appearance of a diffraction peak at q_z = 5.6 nm^{-1} in OOP profile indexed (100)' suggests that ITIC also exhibits bimodal lamellar stacking in face-on and edge-on directions. A corresponding lower stacking distance (d = 1.12 nm) indicates that the lamellar stacking of ITIC is tighter in the OOP direction. These results are consistent with previous studies for as-cast or 150°C annealed thin films.[15,25] At 240°C annealing temperature, the orientation of the molecules changes strongly towards edge-on with typical (100) diffraction peak at q_z = 4.3 nm^{-1} in the OOP profile. This corresponds to a lamellar d-spacing of 1.46 nm and crystal coherence length (CCL) of 14.2 nm. Several spectral signatures indicate a change in the polymorph with the disappearance of the broad π–π stacking peak in OOP, and the appearance of a bright off-axis diffraction peak in the corresponding pattern at (2.93, 6.01) nm^{-1} revealing a lamellar stacking of nearly edge-on oriented ITIC crystallites tilted by 26° from the surface normal. These analyses reveal that the high mobility of ITIC films show a preferential lamellar stacking in both edge-on and tilted edge-on orientations after annealing at 240°C.

Compared to ITIC, ITIC-Th shows relatively similar poor crystallinity at 100°C (**Figure 8**), with a bimodal lamellar stacking in both face-on and edge-on orientations highlighted by a broad π–π stacking peak (010) in OOP at q_z = 18.3 nm^{-1} and lamellar stacking peak (100) in both IP and OOP directions. At 150°C, ITIC-Th exhibits much brighter and sharper scattering peaks, demonstrating a higher degree of crystallinity with a CCL of 8 nm. According to previous reported similar IP and OOP profiles for thermal annealed ITIC-Th films at 130°C, the diffraction peaks located at q_{xy} = 4.6, 9.3 and 13.5 nm^{-1} in the IP profile are indexed (100), (200) and (300).[25a] These diffraction peaks correspond to the in-plane lamellar stacking of ITIC-Th with a lattice constant of 1.35 nm. The intense (010) diffraction peak in the OOP direction corresponds to the π–π stacking with d-spacing of 3.8 nm. The presence of others diffraction peaks at q_{xy} = 3.4, 6.6 and 10 nm^{-1}, indexed from (001) to (003) in the IP profile, suggests the existence of a second structural ordering with a lattice constant of 1.84 nm. As already reported, the occurrence of three orders of diffraction peak suggests an ordered long-range structure in-plane direction along the backbone direction.[25a] All these observations indicate that ITIC-Th crystalline domains are predominantly face-on oriented. Nevertheless, with a typical (100) diffraction peak as intense and narrow in IP as OOP profiles implies that ITIC-Th also exhibits a bimodal lamellar stacking in both face-on and edge on directions. With peak positions at q_{xy} = 4.64 and q_z = 4.34 nm^{-1}, ITIC-Th crystallites show an edge-on orientation at 150°C corresponding to a lamellar d-spacing of 1.3-1.4 nm and a CCL of 8 nm. Such lamellar crystallite size is in accordance with small grains observed by AFM. We can thus conclude that ITIC-Th molecules adopt a bimodal lamellar stacking in both face-on and edge-on orientations in the high mobility phase after thermal annealing at 150°C.

For the fluorinated compound ITIC-4F, we observe the most significant changes between low (100°C) and high temperature annealing (200°C) in the 2D-GIXD profiles compared to ITIC and ITIC-Th. A poor self-organization behavior is observed at 100°C with a weak OOP π–π scattering reflection at q_z = 17.8 nm^{-1} corresponding to a d-spacing of 0.35 nm.[8b] Interestingly,

the ITIC-4F film exhibits diffraction peaks located at q = 3.5-3.9 nm^{-1} in IP and OOP highlighting a bimodal lamellar stacking in both face-on and edge-on directions. It is of main importance to mention here that ITIC-4F films were deposited on PEDOT:PSS that may explain a different ordering compared to recent results shown on films deposited on ZnO buffer layer, for which ITIC-4F films were found amorphous.[8b] Such morphological difference is confirmed in the present study by **Figure S13**. At 200°C, ITIC-4F films are composed of highly ordered crystallites as noted by an intense and narrow diffraction peak indexed (100) at q_z = 4.46 nm^{-1} in OOP profile. It is attributed to the edge-on lamellar stacking of ITIC-4F with a lattice constant of 1.56 nm and a CCL of 21.5 nm. The appearance of bright off-axis diffraction peaks along a 45° inclined axis reveals a lamellar stacking of ITIC-4F crystallites tilted by 45° from the surface normal (**Figure S14**). The corresponding lamellar d-spacing is 1.51 nm for a CCL of 22.6 nm in accord with the 20 nm diameter grains observed by AFM. The results reveal that ITIC-4F adapts in the high mobility regime a preferential lamellar stacking in both edge-on and tilted edge-on molecular plane orientations in thin film annealed at 200°C with crystallites of 20 nm in size.

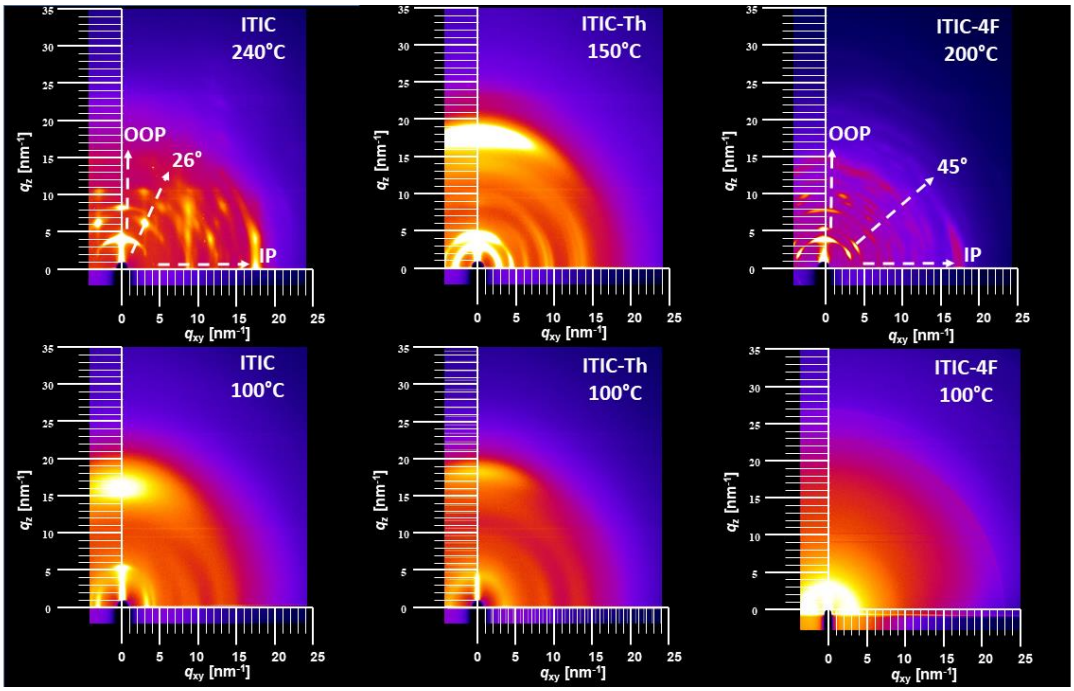

Figure 7. 2D-GIXRD patterns of ITIC, ITIC-Th and ITIC-4F thin films as function of thermal annealing temperature.

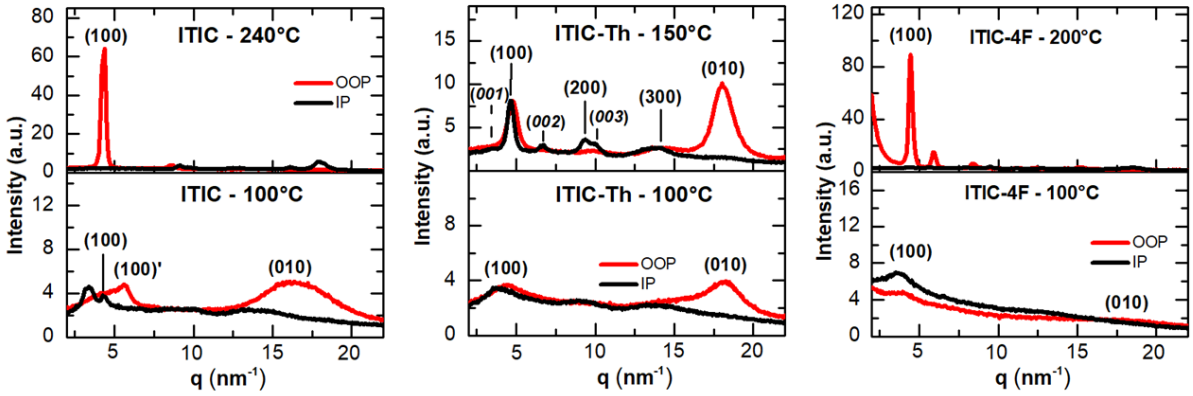

Figure 8. 2D-GIXRD profiles in plane (IP) and out of plane (OOP) of ITIC, ITIC-Th and ITIC-4F thin films as function of thermal annealing temperature.

2.4 Discussion

Compared to fullerene acceptors with pronounced isotropic electron transport, intrinsic charge transport of NFAs is more complex as these materials have anisotropic charge transport as well as temperature depending polymorphs.[8b,9,23] For ITIC derivatives it was first shown that two main polymorph states exist below and above its glass transition temperature (T_g = 180°C), while L. Ciammaruchi *et al.* showed later that there are even additional polymorph phases below T_g for ITIC, which is in accordance with our observation here.[9,26] Furthermore ITIC-Th, for which we studied the first time temperature depending ordering, also shows a second polymorph phase at 100°C below T_g. The combined analysis of electronic transport and molecular ordering performed here revealed that there is a material dependent correlation between polymorph phases and high and low mobility regimes, respectively. For example, ITIC shows the highest mobility in high temperature phases at 240°C, while in the two low

temperature phases at 100°C and 150°C, respectively, first enhanced and then reduced electron mobility was found. Compared to this, ITIC-Th shows a reverse evolution of electron mobility with the changes in phase; indeed, while the low temperature phase produces already relatively high mobility, the phase at 100°C induces a clear drop in electron mobility before reaching the high mobility regime at 150°C. In the case of ITIC-4F we only found a low temperature phase up to 150°C corresponding to the low mobility regime, while the pronounced phase transition at 200°C generates the high mobility phase only. Looking more in detail on the specific parameters governing the charge transport, i.e. type of aggregates, degree of ordering as well as a molecule orientation in the transistor channel, we learned that the charge transport in all phases is mainly dominated by the degree of order and the amount of J-aggregates that is molecule specific over the whole temperature range. Interestingly, the orientation of the molecule inside the nanocrystals, i.e. edge-on or face-on, relative to the transistor channel has only minor impact on the charge transport inside the layers. Indeed, ITIC-Th and ITIC films show in the high mobility regime at 150°C and 240°C, respectively, clear difference in molecule orientation, namely face-on for ITIC-Th and preferably edge-on for ITIC, while the coherence length are comparable between 8-14 nm. Finally, ITIC-4F delivers the highest electron mobility with 3.7×10^{-2} $cm^2/V.s$ in the phase at 200°C, which is characterized by 20 nm sized predominantly edge-on crystallites. Taking into account that this value is about 3 times higher than those of ITIC and ITIC-Th, we may address the superior performance of ITIC-4F to the fluorination of the end groups that promotes not only strongly intermolecular coupling but also higher degree of crystallinity.

Our results also showed that the optimal electron mobility of the three FREAs is more than two orders of magnitude higher than the values measured in polymer blends used for high efficiency solar cells.[4,22b,25b,27] This may be addressed to the additional disorder induced by the presence of the polymer, but mainly to the fact that thermal annealing of the blends is usually limited to 100°C and ultimately by the temperature, tolerated by the substrate, that is typically 150°C for

PET.[28] Thus there is a clear need of designing new NFAs that can reach their optimal transport properties within the temperature regime that can be applied to process organic solar cells, i.e. between 80°C to 140°C. Interestingly we recently show that ITIC blended with the PBDB-T polymer undergoes a polymer-specific induced semi-crystalline phase, promoted by additives and thermal annealing at 100°C only.[29] For the implementation of blend layers in solar cells and to enhance the electron mobility in the acceptor phase, it is therefore of prime importance to consider how the acceptors interacts with the polymer.

In order to design acceptors with intrinsically high electron mobility and thus high J-aggregation and ordering at low temperature, one has to consider more in detail how the molecule structure impact the intermolecular interaction. Based on crystal structures, it is found that IDTT acceptors can organize in two basic crystallization motifs: edge-to-face or face-to-face where face-to-face packing is driven primarily by π-π interactions between end groups.[8] In first instance, both packing motifs can potentially co-exist in pristine thin films or in bulk heterojunction active layers, since film formation is rapid. Nevertheless, previous experimental results through GIWAXS and molecular dynamics simulations have concluded that face-to-face packing is the dominant form of packing in thin films.[7b,7c,8,30] Responsible for these aggregations is the *π–π* stacking between end-groups connecting the backbone of the acceptors while the backbone stacking is reduced due to the large steric hindrance of two bulky 2-ethylhexyl side chains on the central unit limiting their electron transport capabilities.[7c,23] In this face-to-face packing formed by interleaved bricks of π-stacked molecules, planar conjugated backbones and high crystallinity are beneficial for intra and inter molecular carrier transport, respectively, corresponding to the high mobility temperature phase of ITIC-4F observed here.[7c,31]

4. Conclusion

By the development of a new unipolar high temperature stable BGBC OTFT structure, we were able to study the electron transport in high temperature polymorphisms of ITIC, ITIC-Th and ITIC-4F. Using an electronic resin BCB deposited as a thin layer on silicon oxide substrate, we have obtained a dielectric treatment that is thermally more robust than current silanization techniques leading to unique unipolar performances. The use of BGBC OTFT structure allowed us to gain annealing temperature-dependent electron mobility maps of each ITIC derivative. Our results reveal that charge transport in thin films is strongly influenced by the annealing temperature that induces molecule specific polymorphism. The highest electron mobilities of 3.7×10^{-2} $cm^2/V.s$ amongst ITIC and its derivatives together with a $I_{on}/I_{off} > 10^6$ is obtained in ITIC-4F films annealed at 200°C, while ITIC and ITIC-Th show similar optimal transport at 240°C and 150°C, respectively, with lower mobilities of 1.3×10^{-2} $cm^2/V.s$. We also showed that the intrinsic electron transport in the three FREAs depends mainly on degree of molecule ordering and J-aggregates together with intermolecular electronic coupling and is less affected by the molecular plane's orientation such face-on or edge-on orientation inside the channel. Considering the small difference in absolute electron mobility compared to the strong impact of temperature-induced mobility, it seems important to design molecules with intrinsically facilitated long rang J-aggregation capacities. We believe that our developed strategy of determining molecular structure dependence on transport and ordering properties in the solid state of pristine materials allow the identification and design of new acceptor materials that exhibit high electron mobilities under industrially relevant temperatures treatments.[32]

5. Experimental Section/Methods

Materials: ITIC, ITIC-Th and ITIC-4F were purchased from 1-material. 4-(dimethylamino) benzenethiol (DABT) was purchased from TCI. Octyltrichlorosilane (OTS) and hexamethyldisilazane (HMDS) were purchase from Sigma-Aldrich. Photosensitive divinyltetramethyldisiloxane-bis(benzocyclobutene) (BCB) is a class of polymer

commercialized by the Dow Chemical Company under the trade name CYCLOTENE™ 4026-46. All chemicals were used as received.

Transistor Fabrication and Characterization: A schematic representation of OTFT architectures and a top view image are shown in Figure 1. Interdigitated source and drain electrodes structured by a lift-off technique were deposited on n-doped silicon wafers covered with thermally grown silicon dioxide (SiO_2). Interdigitated electrodes were formed by 30 nm of gold (Au) and 10 nm of an adhesion layer of indium tin oxide (ITO). Such interdigitated TFT structures were purchased from Fraunhofer (Germany) with a channel lengths L to channel width W ratio of 20/10000 µm or 10/10000 µm. The capacitance per unit area of 230 nm thick SiO_2 dielectric layers was 14×10^{-9} F.cm^{-2}. Prior the deposition of surface modifying agents, the substrates were consecutively cleaned by ultra-sonication with acetone, ethanol and rinsed with deionized water. The SiO_2 substrates were then dried and treated with final UV-ozone plasma for 15 min at 80°C. Modified Au drain/source electrodes were realized with a DABT monolayer where the thiol group of the benzenethiol derivative is attached to a gold surface. After cleaning, the substrates were immersed 10 min in a 1×10^{-2} mol/l solution of DABT in acetone, and then successively rinsed with toluene, acetone and ethanol for a couple of minutes.

The SiO_2 dielectric surface was then passivated by dip-coating a self-assembled monolayer (SAM) of HMDS or OTS, or by spin-coating a hydroxyl-free polymer BCB as thin buffer layers. OTS layers were formed by soaking the TFT substrates in a 5 mM toluene solution of OTS overnight in a dry N_2-filled glovebox. Trimethylsilation of the Si/SiO_2 surface by HMDS was carried out by dipping the TFT substrates in HMDS solution at room temperature in a closed container overnight. Compared to pristine Si/SiO_2 substrates, the capacitance per unit area of HMDS- and OTS-modified dielectric layers increases slightly to 14.5×10^{-9} F.cm^{-2}. For the passivation by BCB, thin polymeric layers were formed and processed from a BCB solution in 1,3,5-trimetylbenzene in a proportion of 1:200, the solution was then spin-coated on top of the substrate at 3000 rpm during 1 min. The BCB thin films were cross-linked at 250°C on a hot

plate for 1 h in a N_2-filled glovebox. The thickness of the resulting BCB passivating layer was measured to 3.5 nm for a capacitance per unit area of BCB-modified SiO_2 substrates of 18.8×10^{-9} $F.cm^{-2}$.

ITIC, ITIC-Th and ITIC-4F solutions were prepared in chlorobenzene at a concentration of 10 mg/mL and stirred overnight at 60°C. After gold and dielectric treatment, the organic solutions were spin-coated with a spin-coater machine from SET Company (model TP 6000) onto the substrates at 1000 rpm during 2 min. After the solution deposition, the coated substrates were annealed on a preheated hot plate (from 100 to 240°C) for 10 min as a post-treatment. Spin-coating and annealing were performed in a nitrogen-filled glove box. Current-voltage characteristics were performed with a Hewlett-Packard 4140B pico-amperemeter-DC voltage source. The mobility values μ were extracted from the saturation region of the transfer curves with the equation:

$$I_{D,sat} = \frac{W}{2L} C_{ox}\mu_{sat} (V_G - V_T)^2 \quad (2)$$

where $I_{D,sat}$ is the drain-source voltage, C_{ox} is the capacitance per unit area of the gate insulator layer, V_G is the gate voltage, V_T is the threshold voltage, and μ_{sat} is the field-effect mobility. All electrical characterization results were performed in nitrogen-filled glove box.

Thin Films Fabrication and Characterization: Film thicknesses were measured by a stylus profilometer (Bruker DEKTAK XT) with a 1 mg force on the probing tip. Capacitance vs. Frequency measurements on the 20 Hz-1 MHz range were carried out with an HP 4284 LCR meter at room temperature. Curves were obtained at 0 V bias (equilibrium condition) with a 30 mV probing signal. The capacitance density C_{ox} (nF/cm^2) was measured from parallel-plate capacitors with 3 varying contact areas. To minimize external noises, measurements were performed inside an opaque faraday box. The surface morphology of NFAs-based layers deposited on BCB-modified SiO_2 substrates was investigated by atomic force microscopy (AFM NTEGRA from NT-MIDT) in tapping mode by using the silicon tips (MikroMash) with

theoretical resonant frequency of 300 kHz and a spring constant of 16 N m^{-1} at room temperature. NFA layers deposited on glass substrates or PEDOT:PSS buffer layers were further analyzed by 2D grazing-incidence X-ray diffractometry (2D-GIXD) with high-brightness synchrotron radiation at BL19B2 in SPring-8. 2D-GIXD measurements were performed using a high-sensitive 2D X-ray detector (PILATUS 300K). The incident angle and wavelength of X-rays were 0.13° and 0.100 nm, respectively.

Supporting Information
Supporting Information is available from the Wiley Online Library or from the author.

Acknowledgements
This project has received funding by the French National Research Agency (ANR) under the project ANR-17-CE05-0020-01 named NFA-15. J.A. and Y.A.A.Q. thank the ANR for PhD funding within the framework of NFA-15 project. P.P. and J.A. received funding from the European Union's Horizon 2020 research and innovation program under the Marie Skłodowska-Curie Grant Agreement No. 713750. They further acknowledge support of the Regional Council of Provence-Alpes-Côte d'Azur, A*MIDEX (No. ANR-11-IDEX-0001-02), and the Investissements d'Avenir project funded by the French Government, managed by the ANR. This work has been also carried out within the framework of a CIFRE PhD grant 2017/0529 to E.B. from the ANRT (Association Nationale de la Recherche et de la Technologie) and the Ministère de l'Enseignement Supérieur, de la Recherche et de l'Innovation, awarded through the company Dracula Technologies (Valence, France). C.V.-A. thanks the Laboratoire d'analyse et d'architecture des systèmes (LAAS-CNRS, UPR 8001) for providing the CYCLOTENE™. The synchrotron radiation experiments were performed at BL19B2 in SPring-8 with the approval of Japan Synchrotron Radiation Research Institute (JASRI) (Proposal 2019B1851). N.Y. received funding from JSPS, Grant-in-Aid for Scientific Research KAKENHI [grant number 19K05289].

Received: ((will be filled in by the editorial staff))
Revised: ((will be filled in by the editorial staff))
Published online: ((will be filled in by the editorial staff))

References

[1] a) Q. Liu, Y. Jiang, K. Jin, J. Qin, J. Xu, W. Li, J. Xiong, J. Liu, Z. Xiao, K. Sun, S. Yang, X. Zhang, L. Ding. *Sci. Bull.* **2020**, *65*, 272. b) Y. Cui, H. Yao, J. Zhang, K. Xian, T. Zhang, L. Hong, Y. Wang, Y. Xu, K. Ma, C. An, C. He, Z. Wei, F. Gao, J. Hou. *Adv. Mat.* **2020**, *32*,

1908205. c) F. Zhao, H. Zhang, R. Zhang, J. Yuan, D. He, Y. Zou, F. Gao. *Adv. Energy Mater*. **2020**, *10*, 2002746.

[2] a) D. Baran, T. Kirchartz, S. Wheeler, S. Dimitrov, M. Abdelsamie, J. Gorman, R. S. Ashraf, S. Holliday, A. Wadsworth, N. Gasparini, P. Kaienburg, H. Yan, A. Amassian, C. J. Brabec, J. R. Durrant, I. McCulloch. *Energy Environ. Sci.*, **2016**, ***9***, 3783. b) B. He, B. Yang, M. A. Kolaczkowski, C. A. Anderson, L. M. Klivansky, T. L. Chen, M. A. Brady, Y. Liu. *ACS Energy Lett.* **2018**, *3*, 1028. c) N. An, Y. Cai, H. Wu, A. Tang, K. Zhang, X. Hao, Z. Ma, Q. Guo, H S. Ryu, H. Y. Woo, Y. Sun, E. Zhou. *Adv. Mater*. **2020**, *32*, 2002122. d) N. Bauer, Q. Zhang, J. J. Rech, S. Dai, Z. Peng, H. Ade, J. Wang, X. Zhan, W. You. *Nano Research*, **2019**, *12*, 2400. e) F. Zhao, H. Zhang, R. Zhang, J. Yuan, D. He, Y. Zou, F. Gao. *Adv. Energ. Mater*., 2020, *10*, 2002746.

[3] a) A. Wadsworth, M. Moser, A. Marks, M. S. Little, N. Gasparini, C. J. Brabec, D. Baran, I. McCulloch, *Chem. Soc. Rev.* **2019**, *48*, 1596. b) C. Yan, S. Barlow, Z. Wang, H. Yan, A. K.-Y. Jen, S. R. Marder, X. Zhan, *Nat. Rev. Mater.* **2018**, *3*, 18003. c) Y. Ma, D. Cai, S. Wan, P. Yin, P. Wang, W. Lin, Q. Zheng. *Natl. Sci. Rev*. **2020**, *7*, 1886. d) Y. Ma, D. Cai, S. Wan, P. Wang, J. Wang, Q. Zheng. *Angew. Chem., Int. Ed.* **2020**, *59*, 21627. e) X. Zhang, L. Qin, J. Yu, Y. Li, Y. Wei, X. Liu, X. Lu, F. Gao, H. Huang. *Angew. Chem., Int. Ed.* **2021**, *133*, 12583. f) H. Liu, Y. Li, S. Xu, Y. Zhou, Z. Li. *Adv. Func. Mater*. **2021**, 10.1002/adfm.202106735. g) X. Zhang, C. Li, L. Qin, H. Chen, J. Yu, Y. Wei, X. Liu, J. Zhang, Z. Wei, F. Gao, Q. Peng, H. Huang. *Angew. Chem., Int. Ed.* **2021**, *133*, 17861. h) J. Cai, X. Zhang, C. Guo, Y. Zhuang, L. Wang, D. Li, D. Liu, T. Wang. *Adv. Func. Mater.* **2021**, *31*, 2102189.

[4] Y. Lin, J. Wang, Z.-G. Zhang, H. Bai, Y. Li, D. Zhu, X. Zhan. *Adv. Mater*. **2015**, *27*, 1170.

[5] W. Zhao, S. Li, H. Yao, S. Zhang, Y. Zhang, B. Yang, J. Hou. *J. Am. Chem. Soc*. **2017**, *139*, 7148.

[6] a) T. J. Aldrich, S. M. Swick, F. S. Melkonyan, T. J. Marks. *Chem. Mater*. **2017**, *29*, 10294. b) J. Hou, O. Inganäs, R. H. Friend, F. Gao. *Nat. Mat.* **2018**, *17*, 119. c) P. Perkhun, W. Köntges,

F. Pourcin, D. Esteoulle, E. Barulina, N. Yoshimoto, P. Pierron, O. Margeat, C. Videlot-Ackermann, A. Guerrero, J. Bisquert, R.R. Schröder, M. Pfannmöller, S. Ben Dkhil, J.-J. Simon, J. Ackermann, *Adv. Energy Sustain. Res*. **2021**, 2000086. d) S. Lu, F. Li, K. Zhang, J. Zhu, W. Cui, R. Yang, L. Yu, M. Sun. *Solar Energy*, **2020**, *195*, 429. e) Q. Fan, W. Su, M. Zhang, J. Wu, Y. Jiang, X. Guo, F. Liu, T. P. Russell, M. Zhang, Y. Li. *Solar RRL*, **2019**, *3*, 1900169.

[7] a) S. Li, L. Ye, W. Zhao, X. Liu, J. Zhu, H. Ade, J. Hou. *Adv. Mater*. **2017**, *29*, 1704051. b) S. M. Swick, T. Gebraad, L. Jones, B. Fu, T. J. Aldrich, K. L. Kohlstedt, G. C. Schatz, A. Facchetti, T. J. Marks. *Chem Phys Chem* **2019**, *20*, 2608. c) S. M. Swick, W. Zhu, M. Matta, T. J. Aldrich, A. Harbuzaru, J. T. Lopez Navarrete, R. Ponce Ortiz, K. L. Kohlstedt, G. C. Schatz, A. Facchetti, F. S. Melkonyan, T. J. Marks. *Proc. Natl. Acad. Sci. U. S. A.* **2018**, *115*, E8341. d) L. Ye, X. Jiao, M. Zhou, S. Zhang, H. Yao, W. Zhao, A. Xia, H. Ade, J. Hou. *Adv. Mater*. **2015**, *27*, 6046. e) D. Deng, Y. Zhang, J. Zhang, Z. Wang, L. Zhu, J. Fang, B. Xia, Z. Wang, K. Lu, W. Ma, Z. Wei. *Nat. Commun*. **2016**, *7*, 13740.

[8] a) G. Han, Y. Guo, X. Song, Y. Wang, Y. Yi. *J. Mater. Chem. C*, **2017**, *5*, 4852. b) T. J. Aldrich, M. Matta, W. Zhu, S. M. Swick, C. L. Stern, G. C. Schatz, A. Facchetti, F. S. Melkonyan, T. J. Marks. *J. Am. Chem. Soc*. **2019**, *141*, 3274.

[9] L. Ciammaruchi, O. Zapata-Arteaga, E. Gutiérrez-Fernández, J. Martin, M. Campoy-Quiles. *Mater. Adv*. **2020**, *1*, 2846.

[10] a) G. Horowitz, *J. Mater. Res.* **2004**, *19*, 1946. b) H. Bristow, K. J. Thorley, A. J. P. White, A. Wadsworth, M. Babics, Z. Hamid, W. Zhang, A. F. Paterson, J. Kosco, J. Panidi, T. D. Anthopoulos, I. McCulloch. *Adv. Electron. Mater*. **2019**, 1900344. c) C. Videlot-Ackermann, J. Ackermann, H. Brisset, K. Kawamura, N. Yoshimoto, P. Raynal, A. El Kassmi, F. Fages. *J. Am. Chem. Soc.*, **2005**, *127*, 16346. d) Y. Didane, G. H. Mehl, A. Kumagai, N. Yoshimoto, C. Videlot-Ackermann, H. Brisset. *J. Am. Chem. Soc.*, **2008**, *130*, 17681. e) Y. Gao, X. Zhang, H. Tian, J. Zhang, D. Yan, Y. Geng, F. Wang. *Adv. Mater*. 2015, *27*, 6753. f) T. Lei, X. Xia, J.-Y. Wang, C.-J. Liu, J. Pei. *J. Am. Chem. Soc*. **2014**, *136*, 2135. g) A. Zen, J. Pflaum, S.

Hirschmann, W. Zhuang, F. Jaiser, U. Asawapirom, J. P. Rabe, U. Scherf, D. Neher. *Adv. Funct. Mater* **2004**, *14*, 757. h) Z. Chen, M. J. Lee, R. S. Ashraf, Y. Gu, S. Albert-Seifried, M. M. Nielsen, B. Schroeder, T. D. Anthopoulos, M. Heeney, I. McCulloch, H. Sirringhaus. *Adv. Mater*. **2012**, *24*, 647. i) P. Sonar, T.-J. Haband, A. Dodabalapur. *Chem. Com*. **2013**, *49*, doi:10.1039/c2cc37131f.

[11] a) Y. Shi, J. Liu, Y. Hu, W. Hu, L. Jiang. *Nano Select*, 2021, 1. b) B. Lucas, T. Trigaud, C. Videlot-Ackermann. *Polym Int.* **2012**, *61*, 374.

[12] a) F. S. Kim, D.-K. Hwang, B. Kippelen, S. A. Jenekhe. *Appl. Phys. Let.* **2011**, *99*, 173303. b) M.-H. Yoon, C. Kim, A. Facchetti, T. J. Marks, *J. Am. Chem. Soc.***2006**, *128*, 12851.

[13] a) F. Yang, C. Li, W. Lai, A. Zhang, H. Huang, W. Li, *Mater. Chem. Front.* **2017**, *1*, 1389. b) J. H. L. Ngai, C. C. M. Chan, C. H. Y. Ho, J. K. W. Ho, S. H. Cheung, H. Yin, S. K. So. *Mater. Adv.*, **2020**, *1*, 891. c) Y. Park, C. Fuentes-Hernandez, X. Jia, F. A. Larrain, J. Zhang, S. R. Marder, B. Kippelen, *Org. Electron.* **2018**, *58*, 290.

[14] a) M. Yoon, K. R. Ko, S.-W. Min, S. Im, *RSC Adv.* **2018**, *8*, 2837. b) L. Jiang, J. Liu, X. Lu, L. Fu, Y. Shi, J. Zhang, X. Zhang, H. Geng, Y. Hu, H. Dong, L. Jiang, J. Yu, W. Hu, *J. Mater. Chem. C* **2018**, *6*, 2419. c) Y. Jiang, Y. Guo, Y. Liu. *Adv. Electron. Mater*. **2017**, *3*, 1700157.

[15] M. Chen, D. Liu, W. Li, R. S. Gurney, D. Li, J. Cai, E. L. K. Spooner, R. C. Kilbride, J. D. McGettrick, T. M. Watson, Z. Li, R. A. L. Jones, D. G. Lidzey, T. Wang. *ACS Appl. Mater. Interfaces* **2019**, *11*, 26194.

[16] Y. Lin, F. Zhao, Q. He, L. Huo, Y. Wu, T. C. Parker, W. Ma, Y. Sun, C. Wang, D. Zhu, A. J. Heeger, S. R. Marder, X. Zhan. *J. Am. Chem. Soc.* **2016**, *138*, 4955.

[17] Y. Kuzumoto, M. Kitamura. *Appl. Phys. Express* **2014**, *7*, 035701.

[18] a) M. Robin, M. Harnois, Y. Molard, E. Jacques. *Org. Electron.* **2016**, *39*, 214. b) X.-H. Zhang, S. P. Tiwari, B. Kippelen. *Org. Electron.* **2009**, *10*, 1133. c) Th. B. Singh, N.

MarjanoviĆ, P. Stadler, M. Auinger, G. J. Matt, S. Günes, N. S. Sariciftci. *J. Appl. Phys.* **2005**, *97*, 083714.

[19] a) X. D. Yang, H. T. Wang, P. Wang, X. X. Yang, H. Y. Mao. *Nanomaterials* **2020**, *10*, 210. b) E. Orgiu, M. A. Squillaci, W. Rekab, K. Börjesson, F. Liscio, L. Zhang, P. Samorì. *Chem. Commun.* **2015**, ***51***, 5414.

[20] Y. Lin, F. Zhao, Q. He, L. Huo, Y. Wu, T. C. Parker, W. Ma, Y. Sun, C. Wang, D. Zhu, A. J. Heeger, S. R. Marder, X. Zhan, *J. Am. Chem. Soc.* **2016**, *138*, 4955.

[21] H. H. Choi, K. Cho, C. D. Frisbie, H. Sirringhaus, V. Podzorov, *Nat. Mater.* **2018**, *17*, 2.

[22] a) Z. Li, S. Dai, J. Xin, L. Zhang, Y. Wu, J. Rech, F. Zhao, T. Li, K. Liu, Q. Liu, W. Ma, W. You, C. Wang, Xi. Zhan. Mater. *Chem. Front.* **2018**, DOI: 10.1039/c7qm00547d. b) T. J. Aldrich, S. M. Swick, F. S. Melkonyan, T. J. Marks. *Chem. Mater*. **2017**, *29*, 10294.

[23] G. Han, T. Hu, Y. Yi. *Adv. Mater*. **2020**, 2000975.

[24] L. Benatto, M. Koehler. *J. Phys. Chem. C* **2019**, *123*, 6395.

[25] a) J. Mai, Y. Xiao, G. Zhou, J. Wang, J. Zhu, N. Zhao, X. Zhan, X. Lu. *Adv. Mater*. **2018**, 1802888. b) Y. Yang, Z.-G. Zhang, H. Bin, S. Chen, L. Gao, L. Xue, C. Yang, Y. Li. *J. Am. Chem. Soc.* **2016**, *138*, 15011. c) Q. Fan, Z. Xu, X. Guo, X. Meng, W. Li, W. Su, X. Ou, W. Ma, M. Zhang, Y. Li. *Nano Energy* **2017**, *40*, 20.

[26] L. Yu, D. Qian, S. Marina, F. A. A. Nugroho, A. Sharma, S. Hultmark, A. I. Hofmann, R. Kroon, J. Benduhn, D.-M. Smilgies, K. Vandewal, M. R. Andersson, C. Langhammer, J. Martín, F. Gao, C. Müller. *ACS Appl. Mater. Interfaces* **2019**, *11*, 21766.

[27] a) F. Yang, C. Li, W. Lai, A. Zhang, H. Huang, W. Li. *Mat. Chem. Frontiers*, **2017**, *1*, 1389. b) D. Xie, T. Liu, W. Gao, C. Zhong, L. Huo, Z. Luo, K. Wu, W. Xiong, F. Liu, Y. Sun, C. Yang. *RRL Solar*, **2017**, *1*, 1700044.

[28] a) Y. Wang, J. Lee, X. Hou, C. Labanti, J. Yan, E. Mazzolini, A. Parhar, J. Nelson, J.-S. Kim, Z. Li. *Adv. Energy Mater*. **2021**, 11, 2003002. b) C.H. Kim, Y. Lee. *Int. J. Precis. Eng.*

Manuf. **2011**, *12***,** 161. c) M. Kaltenbrunner, M S. White, E. D. Głowacki, T. Sekitani, T. Someya, N. S. Sariciftci, S. Bauer. *Nat. Com.* **2012**, *3*, 770.

[29] W. Köntges, P. Perkhun, J. Kammerer, R. Alkarsifi, U. Würfel, O. Margeat, C. Videlot-Ackermann, J.-J. Simon, R. Schröder, J. Ackermann, M. Pfannmöller. *Energy Environ. Sci.*, **2020**, 13, 1259

[30] D. Yan, W. Liu, J. Yao, C. Zhan, *Adv. Energy Mater.* **2018**, *8*, 1800204.

[31] a) A. Salleo. *Mater. Today* **2007**, *10*, 38. b) G. R. Hutchison, M. A. Ratner, T. J. Marks. *J. Am. Chem. Soc.* **2005**, *127*, 16866.

[32] Y. A. Avalos-Quiroz, O. Bardagot, Y. Kervella, C. Aumaître, L. Cabau, A. Rivaton, O. Margeat, C. Videlot-Ackermann, U. Vongsaysy, J. Ackermann, R. Demadrille. *Chem Sus Chem*, **2021**, *14*, 3502-3510.

Exploring charge transport in high temperature polymorphism of ITIC derivatives in simple processed unipolar bottom contact organic field-effect transistor

Yatzil Alejandra Avalos Quiroz, Tomoyuki Koganezawa, Pavlo Perkhun, Elena Barulina, Carmen M. Ruiz, Jörg Ackermann, Noriyuki Yoshimoto, Christine Videlot-Ackermann**

By the development of a new unipolar high temperature stable BGBC OTFT structure, the electron transport in high temperature polymorphisms of ITIC, ITIC-Th and ITIC-4F is studied. An annealing temperature-dependent electron mobility map is obtained for each molecule highlighting that the intrinsic electron transport depends mainly on degree of molecule ordering and J-aggregates together with intermolecular electronic coupling.

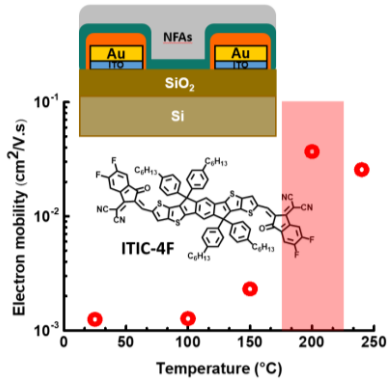

Supporting Information

Exploring charge transport in high temperature polymorphism of ITIC derivatives in simple processed unipolar bottom contact organic field-effect transistor

Yatzil Alejandra Avalos Quiroz, Tomoyuki Koganezawa, Pavlo Perkhun, Elena Barulina, Carmen M. Ruiz, Jörg Ackermann, Noriyuki Yoshimoto, Christine Videlot-Ackermann**

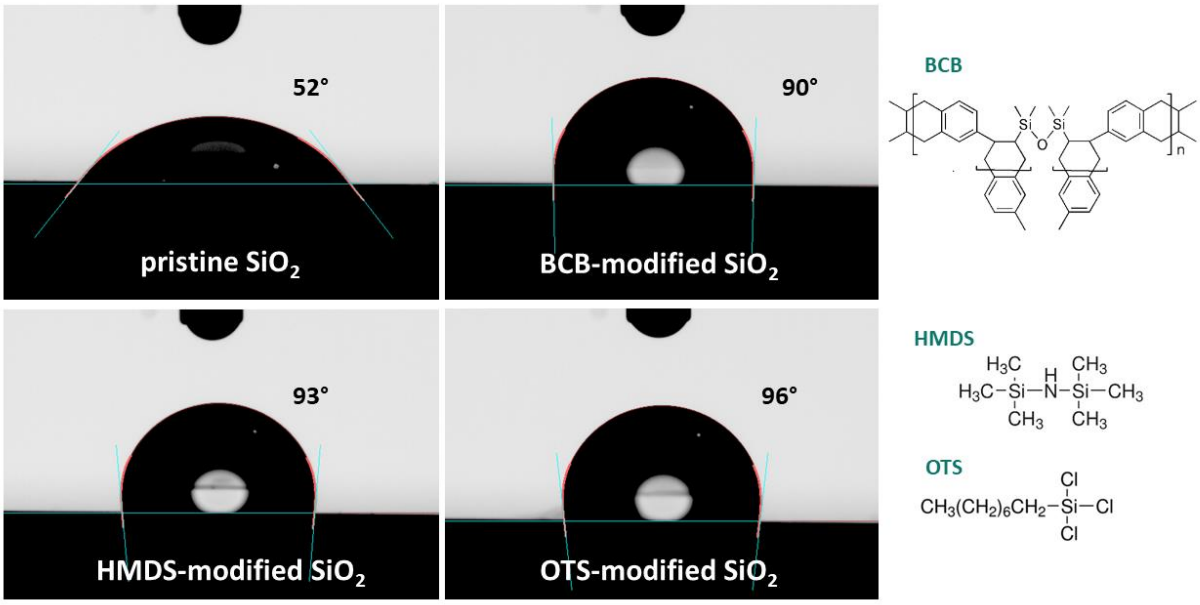

Figure S1. Water contact angle images of the water on the surface of pristine SiO_2 and modified SiO_2 surfaces. Chemical structure of BCB, HMDS and OTS.

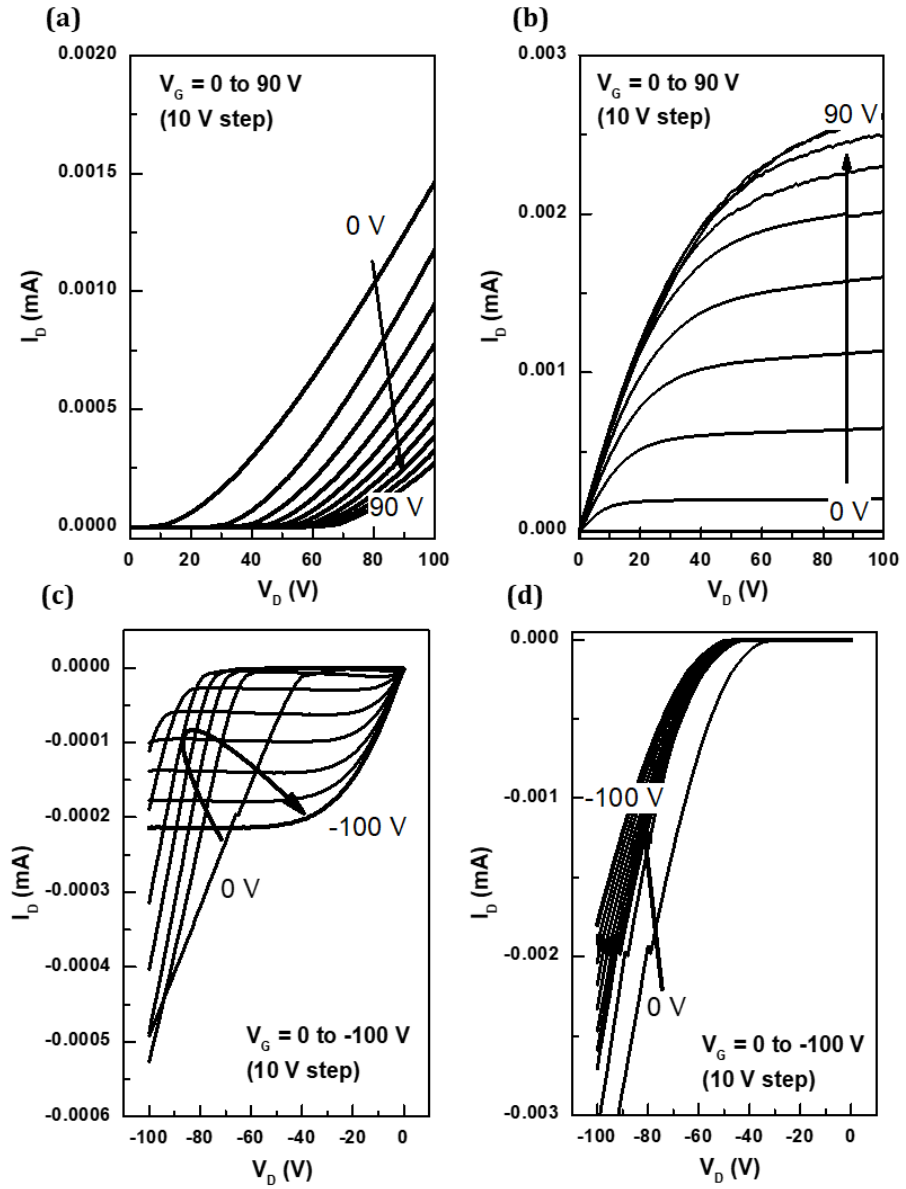

Figure S2. Output characteristics of as-cast ITIC in BGBC OTFTs: on pristine gold electrodes (a,c) and on DABT-treated gold electrodes (b,d) under positive and negative bias. SiO_2 surfaces were unmodified.

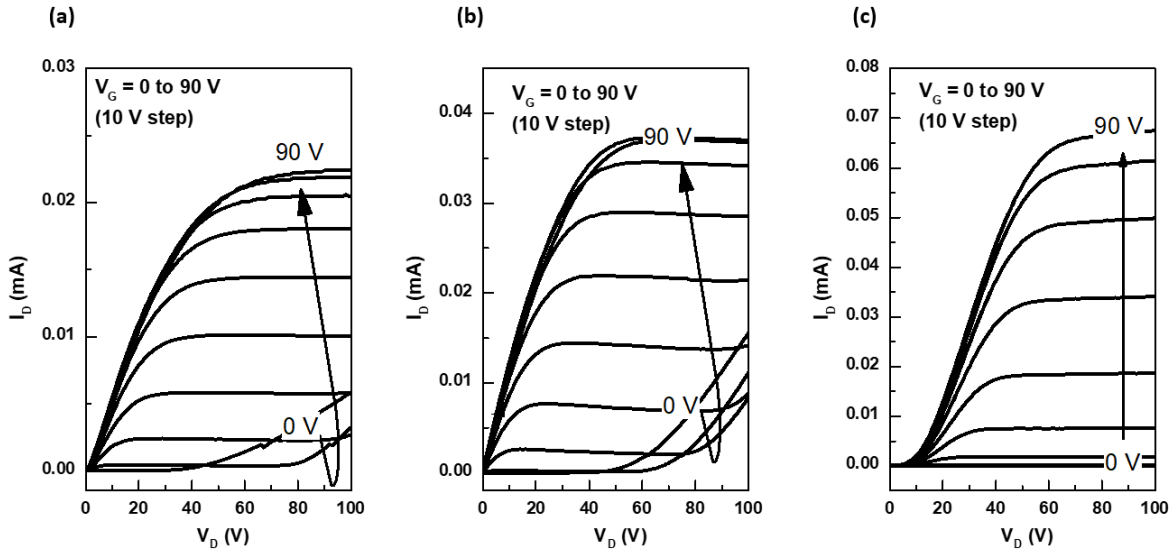

Figure S3: Output characteristics in positive bias of as-cast ITIC films in BGBC OTFTs with DABT-treated gold electrodes and treated SiO_2 dielectric by: (a) HMDS, (b) OTS and (c) BCB.

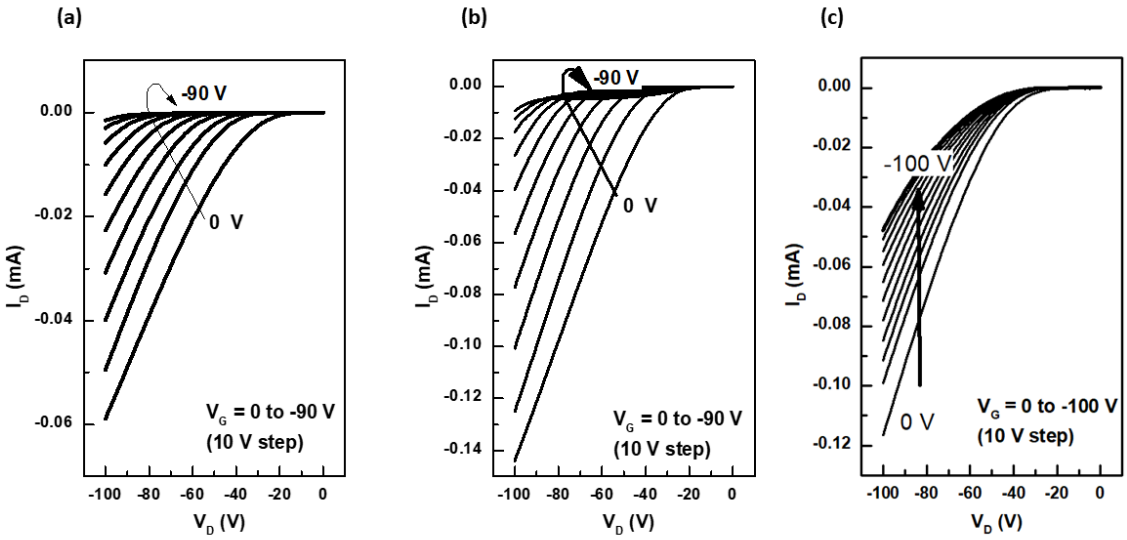

Figure S4. Output characteristics in negative bias of as-cast ITIC films in BGBC OTFTs with DABT-treated gold electrodes and treated SiO_2 dielectric by: (a) HMDS, (b) OTS and (c) BCB.

Table S1. Electron transport parameters of ITIC films (as-cast or post-annealed at 240°C) evaluated in BGBC OTFTs based on DABT-treated gold electrodes and pristine or modified SiO_2 dielectric.

passivation		Temp. (°C)	μ (cm^2/V.s)	V_T (V)	Transport
electrodes	dielectric				
DABT	pristine	as-cast	$1.3 \pm 0.9 \times 10^{-4}$	5.5 ± 3.7	unipolar (electron)
		240°C	$3.3 \pm 2 \times 10^{-4}$	13.7 ± 6.1	
DABT	HMDS	as-cast	$1.4 \pm 0.2 \times 10^{-3}$	7.3 ± 3.4	ambipolar
		240°C	$2.4 \pm 0.9 \times 10^{-3}$	9.7 ± 3.6	
DABT	OTS	as-cast	$1.5 \pm 0.2 \times 10^{-3}$	19.2 ± 5.7	ambipolar
		240°C	$4.9 \pm 0.6 \times 10^{-3}$	23.3 ± 1,2	
DABT	BCB	as-cast	$3.1 \pm 1.1 \times 10^{-3}$	16.6 ± 5.4	unipolar (electron)
		240°C	$1.3 \pm 0.4 \times 10^{-2}$	15 ± 7.7	

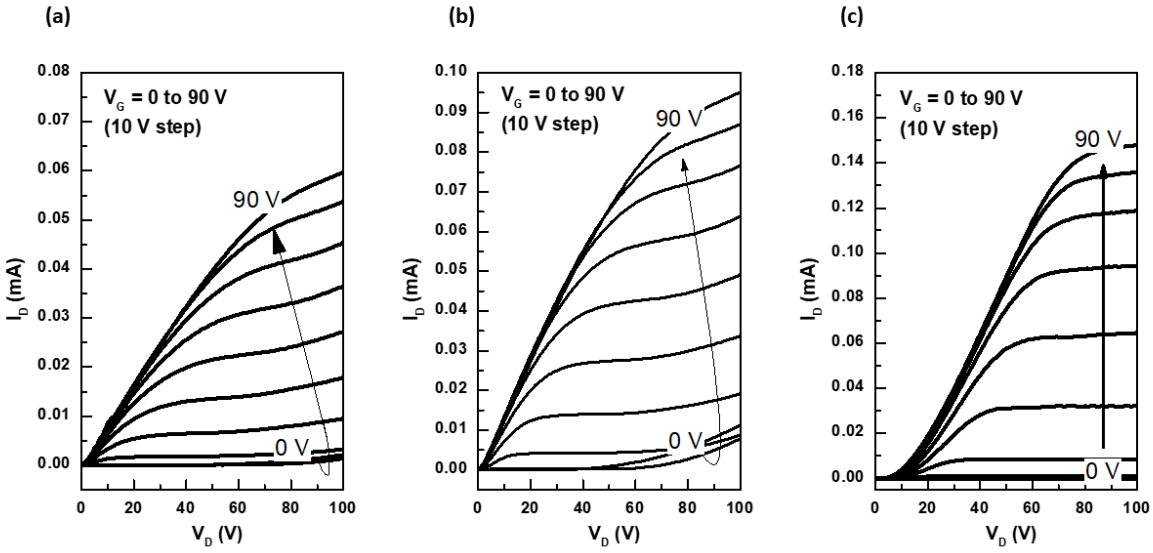

Figure S5. Output characteristics in positive bias after 240°C thermal post-annealing of ITIC films in BGBC OTFTs with DABT-treated gold electrodes and treated SiO_2 dielectric by: (a) HMDS, (b) OTS and (c) BCB.

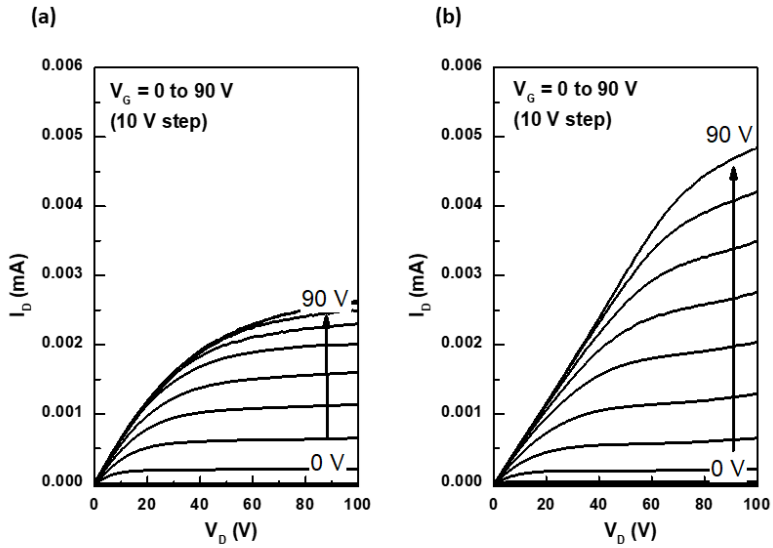

Figure S6. Output characteristics of ITIC films in BGBC OTFTs on unmodified SiO_2 but with DABT-treated gold electrodes: (a) as-cast and (b) post-annealed at 240°C, 10 min.

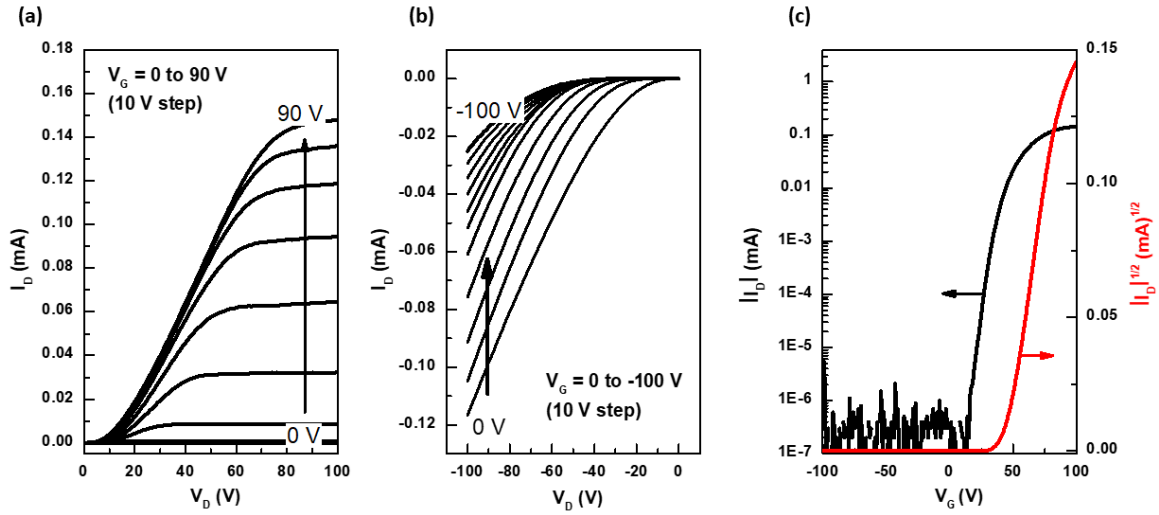

Figure S7. Output (a,b) and transfer (c) characteristics of ITIC post-annealed at 240°C in BGBC OTFTs with BCB-modified SiO_2 and DABT-treated gold electrodes.

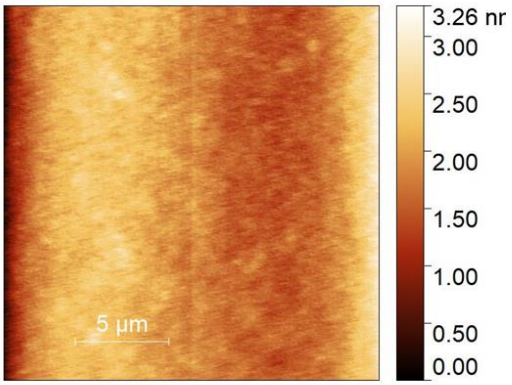

Figure S8. Atomic force microscopy (AFM) image of BCB-modified SiO_2 surface with a root-mean-square surface roughness (rms) of 0.4 nm. Size: 10 µm×10 µm.

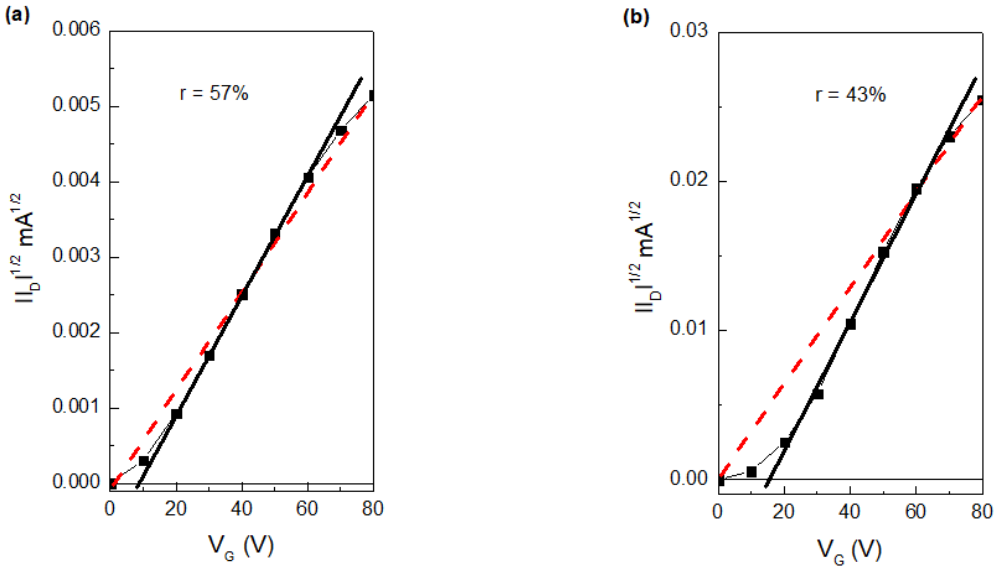

Figure S9. Detailed transfer characteristics of as-cast (a) and 200°C post-annealed (b) ITIC-4F in BGBC OTFTs with BCB-modified SiO_2 and DABT-treated gold electrodes. The black lines indicate the slope used in calculation of the extracted mobility (µ). The red dashed lines represent the slope of electrically equivalent ideal FETs delivering the maximum channel conductivity at $|V_G|$ max but exhibiting correct linear characteristics. The measurement reliability factor, r, in the saturation regime is the ratio squared, expressed in %, of the slopes of the red dashed line and black line.

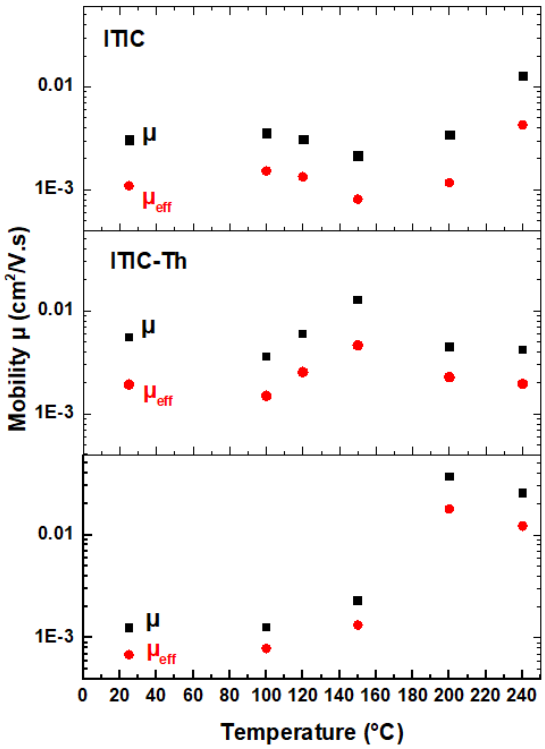

Figure S10. Extracted (μ) and effective (μ_{eff}) mobility values of ITIC, ITIC-Th and ITIC-4F for different post-annealing temperatures of thin films. The measurement reliability factors, r, are 35-45% for ITIC, 25-40% for ITIC-Th and 50-70 % for ITIC-4F.

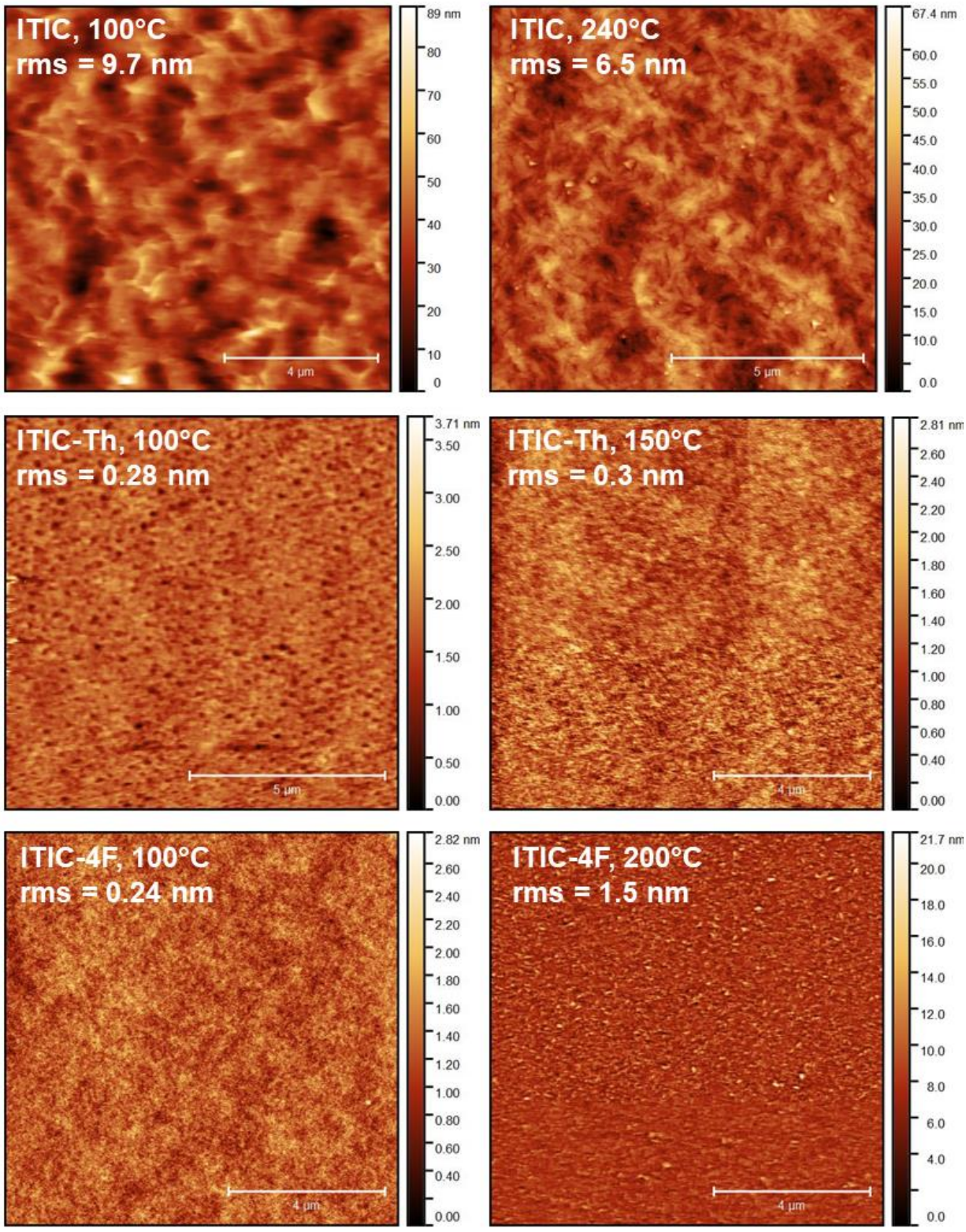

Figure S11. AFM topography images of ITIC, ITIC-Th and ITIC-4F n-type semiconductor molecules deposited on BCB-modified SiO_2 surfaces.

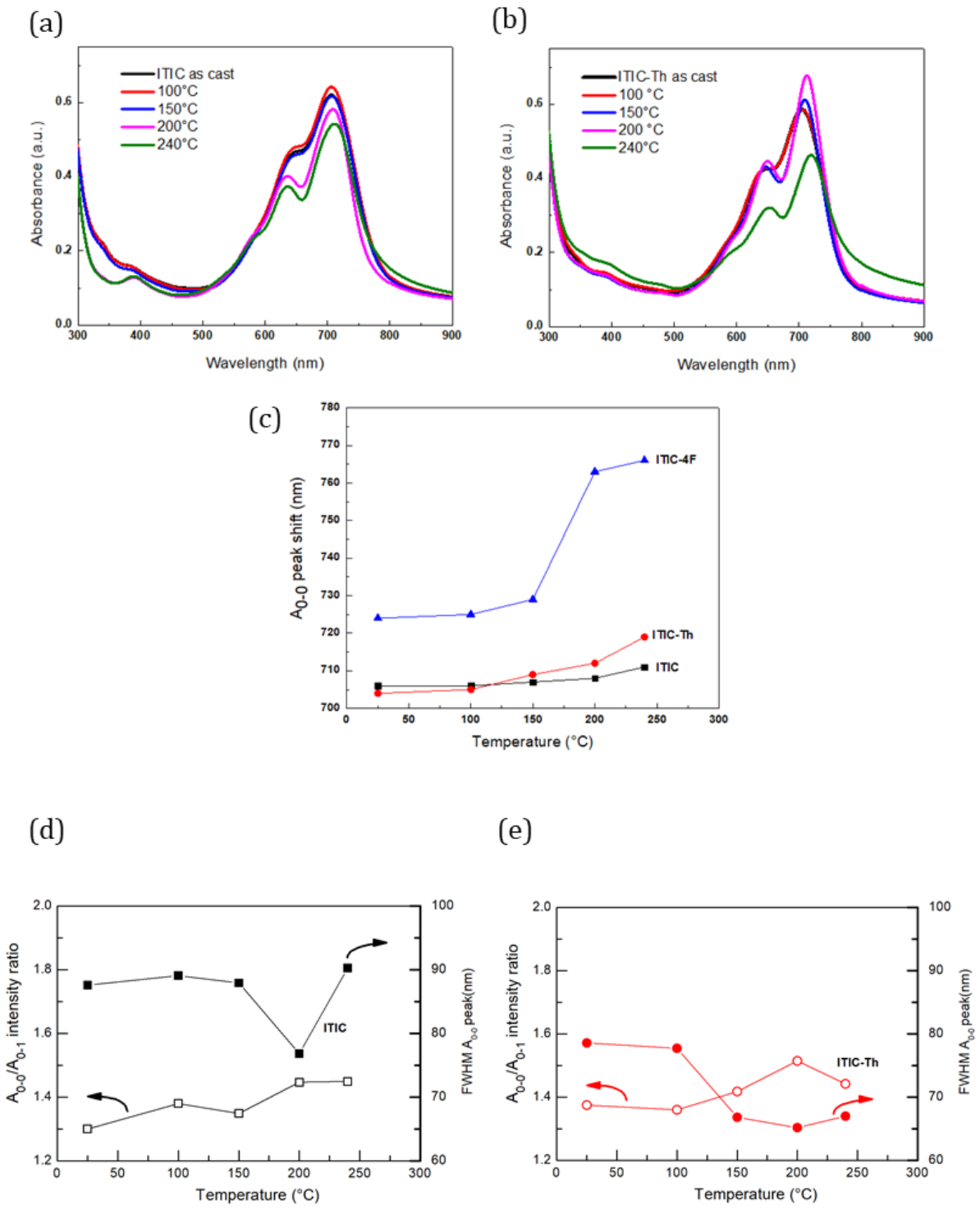

Figure S12. Absorption spectra of ITIC (a) and ITIC-Th (b) thin films as function of the annealing temperature and A_{0-0} peak shift compared to ITIC-4F (c). A_{0-0}/A_{0-1} intensity ratio and FMHW of A_{0-0} peak for ITIC (d) and ITIC-Th (e).

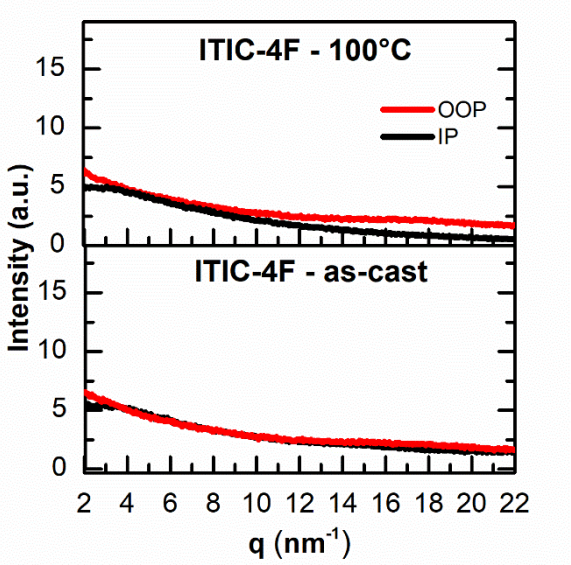

Figure S13. 2D-GIXRD profiles in plane (IP) and out of plane (OOP) of ITIC-4F thin films deposited on ZnO buffer layer.

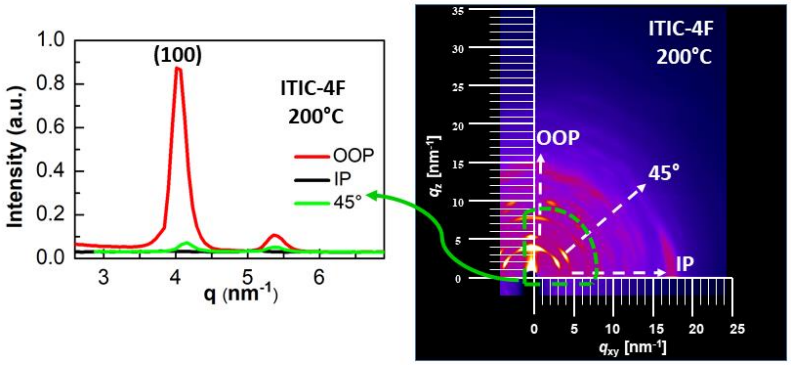

Figure S14. Zoom-in of 2D-GIXRD profiles in plane (IP), out of plane (OOP) and along the 45° direction of ITIC-4F thin films thermal annealed at 200°C.